Journal of Computational Physics 508 (2024) 113030

Contents lists available at ScienceDirect

Journal of Computational Physics

journal homepage: www.elsevier.com/locate/jcp

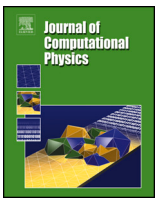

Ten-moment fluid model with heat flux closure for gasdynamic flows

Derek A. Kuldinow [*,1], Yusuke Yamashita [2], Adnan R. Mansour [1], Kentaro Hara [3]

Department of Aeronautics and Astronautics, Stanford University, 496 Lomita Mall, Stanford, CA, 94305, USA

ARTICLE INFO

Keywords:
Higher-order moment methods
Non-equilibrium gas dynamics
Fluid moment closures
Computational fluid dynamics

ABSTRACT

The gasdynamic 10-moment equations are revisited, applying a Chapman-Enskog type expansion to achieve the closure for heat flux. The resulting gradient-based closure performs favorably against previously employed closures in regions of shocks when compared to the kinetic results obtained from Direct Simulation Monte Carlo simulations. The 10-moment model can capture finite kinetic effects due to non-Maxwellian velocity distribution functions, as compared to the 5-moment Navier-Stokes equations, and remains hyperbolic-parabolic with real wave speeds under all initial conditions. Self-consistent kinetic boundary conditions are derived without consideration of a distinct Knudsen layer. The model is applied to a number of canonical gasdynamics problems in one and two dimensions such as steady normal and oblique shocks, as well as the Sod shock tube problem.

1. Introduction

Fluid models are popular in the fields of gas and plasma dynamics, particularly due to their computational cost advantage over kinetic models [1,2]. This efficiency is achieved by solving for the local bulk properties of the flow as opposed to tracking myriad macroparticles directly. One of the major challenges in fluid models is capturing inherently kinetic effects that result in non-Maxwellian velocity distribution functions (VDFs), which arise at higher Knudsen numbers when particles are not able to fully equilibrate. Such flows are encountered in various rarefied gases, including semiconductor manufacturing processes [3], high-altitude flights [4] and many laboratory and astrophysical plasma environments [5,6]. Development of fluid models that can better capture finite kinetic effects can greatly enhance the predictive modeling capabilities of studying systems far from equilibrium.

Typical fluid models are derived by taking the zeroth, first, and contracted second moments of a kinetic transport equation, such as the Boltzmann equation, yielding transport laws for mass, momentum, and energy, respectively. The description of the fluid is complete when the transport laws are coupled with a collision operator that defines the sources and sinks of fluid quantities. Higher-order moment models retain additional moments of the transport equation, which correspond to deviations from an isotropic Maxwellian VDF; the behavior of these equations is described in fundamental textbooks [7–9]. Higher-order moment models (HOMMs) are an attractive approach for handling continuum-kinetic transition regimes because they maintain a hyperbolic form

* Corresponding author.
E-mail address: kuldinow@stanford.edu (D.A. Kuldinow).
[1] Ph.D. Candidate, Stanford University.
[2] Postdoctoral Fellow, Stanford University.
[3] Assistant Professor, Stanford University.

https://doi.org/10.1016/j.jcp.2024.113030
Received 27 June 2023; Received in revised form 30 January 2024; Accepted 16 April 2024

Available online 18 April 2024

similar to the classic Euler and Navier-Stokes (NS) equations, but can directly capture the evolution of a non-Maxwellian distribution function. The fundamental obstacle of fluid moment models, however, is the closure problem. The closure problem arises because the transport equations inevitably require information about the next higher-order moment, which is not explicitly solved for in the system. Oftentimes, an assumption must be made about the VDF to allow for the closure of the higher-order terms that appear in the fluid formulation. The most physically accurate and computationally achievable methods for achieving closure has been a subject of much research [8,10–14], though some recent works have also neglected heat flux and higher order moments [15–17].

Intuitively, capturing more moments of the distribution function should only increase the fidelity of the simulation, since more information about the VDF is retained. However, the description of the set of partial differential equations (PDEs) produced by HOMMs would not be complete without examining their classification as hyperbolic, parabolic, or elliptic. When constructing HOMMs, the PDEs may have a combination of advection (first-order), diffusion (second-order), and source terms. The advection term is usually referred to as the inviscid flux, the diffusion term usually arises from viscous (collisional) effects, and the source terms can be linear or nonlinear depending on the collisional and external processes that are taken into account. The fluxes correspond to the transport of information through the system and are thus dependent on gradients of flow quantities, while sources are typically comprised of external body forces or local collisional effects. These two terms are often dealt with separately since they are fundamentally different processes; the discussion of hyperbolicity will only consider the inviscid flux terms because they primarily contain the spatial gradients that determine the form of the PDE. However, a full solution to the set of PDEs must also take into account the viscous fluxes as well as sources terms, which can make the resulting PDE linear, parabolic, or hyperbolic.

The key challenge for HOMMs is whether the constructed PDE is well-posed. The criteria for a well-posed, time-dependent set of PDEs are that (i) a solution exists, (ii) the solution is unique, and (iii) the solution varies continuously when varying initial conditions. The eigenvalues of the set of PDEs can classify it as well-posed or ill-posed depending on the conditions of the problem. For instance, if the eigenvalues are all real, the initial value problem is well-posed, and thus admits a unique solution under all initial conditions. Such *hyperbolic* PDEs have eigenvalues, eigenvectors, and characteristics, which can be interpreted as information propagating at various speeds through the system, thus generating wave-like solutions. For an ill-posed initial value problem, when one tries to propagate the system forward in time, solutions may not always exist without knowing conditions at later times, and any solution may not be unique. For specific HOMMs, one may find the eigenvalues of the inviscid fluxes to be complex, resulting in an ill-posed initial value problem and a loss of hyperbolicity. While some HOMMs are still usable within their domain of hyperbolicity [18], the loss of hyperbolicity with certain initial conditions limits the applications of such models. As shown later, when higher-order moments are considered, the closure becomes critical as the Knudsen number increases, i.e., the flow becomes less collisional. The higher-order moments (e.g., heat flux) are often diffusive (second-order) in nature. Hence, the flux terms in HOMMs can become a set of hyperbolic-parabolic equations rather than purely hyperbolic. A physical justification for this form is provided in Section 2.3.2.

One of the most well-known closures was proposed by Grad [8] and describes the VDF in terms of polynomial expansions about the equilibrium Maxwellian VDF. Having the Maxwellian VDF as the leading-order term is physical because according to Boltzmann's H-theorem, the Maxwellian VDF is the distribution that results in maximum entropy in the presence of intraspecies binary collisions. In other words, through many binary collisions, any particle velocity distribution will relax to a Maxwellian VDF. Thus, with sufficient collisions, the distribution will be near-Maxwellian and so the Maxwellian VDF can be taken as an equilibrium solution around which perturbations can be made for arbitrary non-Maxwellian VDFs. Grad's 13-moment system, however, can suffer from a breakdown of hyperbolicity due to the inviscid flux equations admitting imaginary eigenvalues when the distribution function is far from equilibrium; furthermore, the form of the distribution function is not positive for all velocities, making it unsuitable as being interpreted as a probability distribution function [19]. Additionally, the 13-moment equations require boundary conditions for the heat flux in addition to the fluid properties (e.g., mass, momentum, and temperature); there have been attempts for physically motivated and accurate boundary condition models [20], but nonphysical results have been observed when far from equilibrium. Further *regularized* versions of Grad's closure have attempted to remedy these shortcomings through further Chapman-Enskog type expansions and have found a number of applications, but they still lack a complete description of boundary conditions and are not guaranteed to remain hyperbolic under all conditions [21,22].

Another option is closure via the assumption of a Pearson IV (PIV) distribution [23]. Compared to the Grad closure, it has been shown to be hyperbolic and positive definite for a wider range of conditions. While the set of PIV distributions includes a Maxwellian VDF in its parameter space, there is no fundamental physical justification (cf. H-theorem) to assume that a PIV VDF should arise under any physical circumstances, particularly for gas dynamics problems. The PIV distribution does not necessarily satisfy maximum entropy nor does it arise from perturbation theory about equilibrium [23]. Furthermore, certain parameters that define the distribution, namely, skew and kurtosis, are not strictly closed-form functions of the central moments of the distribution. For this reason, iterative solvers are typically used to determine these parameters in terms of lower-order moments, allowing for the calculation of higher-order moments [13]. Analytical approximations have also been used, but are employed as a numerical convenience rather than a result derived from first principles [23].

In the Quadrature Method of Moments (QMOM), the distribution function is instead assumed to be the weighted sum of N kernel functions (nodes). Thus, closure is obtained through the ansatz of specifying the distribution function. One option is to use a Dirac delta kernel, where the $2N$ unknowns (weights and positions of the nodes) are then iteratively solved for using a set of $2N$ known moments through a nonlinear set of equations [24,25]. Another option is to use a Gaussian kernel, which allows for nonzero VDF tails at the cost of increasing the number of equations to $2N + 1$; this formulation is useful when considering reactions facilitated by high-energy tail populations [26]. However, it has been observed that results obtained using QMOM may converge slowly with the number of nodes, and furthermore have been observed to exhibit numerical artifacts (e.g., subshocks, oscillations) dependent on number of nodes, grid resolution, and convergence tolerance [27,28].

The search for a more robust physically-motivated closure has led to the development of so-called maximum entropy methods, by assuming a form of the distribution function to mandate stability and satisfy the H-theorem. Such methods have shown great success in their ability to reconstruct a distribution function and capture particle dynamics [12,29,30]. However, the equations can admit arbitrarily high wavespeeds requiring a restrictively small timestep and often involve iterative optimization, which can garner a high computational cost, although approximate interpolative techniques have been posed as a way to circumvent the costly calculations [30,31]. Furthermore, Junk showed that beyond the 10-moment system, there are physically-realizable sets of the macroscopic moments (density, pressure, heat flux etc.) for which there is no valid maximum-entropy distribution [32,33]. Thus, within the hierarchy of physically-motivated maximum entropy models, the 10-moment system captures the most information with the distribution function still guaranteed to exist (and, in fact, has an analytical form), and that all of the inviscid evolution equations remain hyperbolic under all physically realizable conditions.

Another important application of the fluid moment models is ionized gases, i.e., plasmas. In particular, the interaction of electric $\left(\vec{E}\right)$ and magnetic $\left(\vec{B}\right)$ fields can create an $\vec{E}\times\vec{B}$ drift thus modifying the plasma transport (e.g., conductivity and diffusivity) in different directions. For the fluid models, typically for electrons, the generalized Ohm's law or drift-diffusion approximation has been widely used [34,35]. However, it has been recently found that such simplified models are unable to capture nonlinear dynamics that lead to deviations from classical theory [34]. The 10-moment model is well-suited to capture shear-driven transport and instabilities in plasmas, since it can explicitly capture the off-diagonal pressure tensor elements which correspond to shear terms. Particularly, the presence of magnetic fields often creates significantly anisotropic distribution functions [7]. However, due to the collective behavior within plasmas and the long-range of the electromagnetic fields, there exist a wide range of *collisionless* phenomena for which the previously discussed methods, which require a collisional ansatz, are invalid. In such regimes, non-local closures are required, which often take the form of specifying a characteristic wavenumber of interaction. This method was pioneered by Hammett and Perkins [36] and has been applied to so-called 'Landau fluid models' which are able to capture phase mixing and Landau damping [37,38]. In addition, the non-local theory has been extended to collisionless energy transport in the 10-moment model for plasmas [39]. In order to apply the 10-moment model to multi-component ionized gases, it is necessary to develop a 10-moment model with non-reacting gases by benchmarking against conventional 5-moment (Navier-Stokes) and kinetic results, which can be obtained using Direct Simulation Monte Carlo (DSMC).

The main challenge of the 10-moment model is the closure for higher-order moment terms which are not explicitly captured, i.e., heat flux, the third velocity moment. In this paper, we employ Chapman-Enskog type expansion using the ellipsoidal-statistical Bhatnagar-Gross-Krook (ES-BGK) collision operator [11], which results in a gradient-based closure for the heat flux. In Section 2, we discuss the governing equations for our fluid and DSMC simulations and describe the details of the heat flux closure. In Section 3, we describe the numerical methods and boundary conditions. In Sections 4–6, we present the results of applying the fluid and kinetic models to canonical gasdynamic problems. The 10-moment model is applied to one- and two-dimensional Riemann problems and the results are compared to those obtained from DSMC and the Navier-Stokes model.

2. Governing equations

In this paper, we compare the 10-moment results with the 5-moment (such as Navier-Stokes, Euler equations) and kinetic (DSMC) results. Performing a qualitative comparison, i.e., benchmarking, requires discussions of the numerical parameters chosen. For benchmarking, we consider a monatomic gas for the working gas ($\gamma = 5/3$, i.e., three degrees of freedom for translational energy) and only collisions between like particles (i.e., one species and no intermolecular collisions). In the DSMC, a variable hard-sphere (VHS) collision model is used. While in DSMC the collisional transport is performed through individual particle collisions, the fluid approach describes the ensemble of particles. Thus, how the microscopic particle collisions lead to the macroscopic effects of collisional drag and momentum and energy transport coefficients (e.g., viscosity and heat flux) in the fluid approach is discussed.

2.1. 10-moment equations

The transport and collisions of particles are described using the kinetic transport equation:

$$\frac{\partial f}{\partial t} + v_i \frac{\partial f}{\partial x_i} + \frac{F_i}{m}\frac{\partial f}{\partial v_i} = C(f), \tag{1}$$

where $f = f(\mathbf{x}, \mathbf{v}, t)$ is the distribution function as a function of position, velocity and time, F_i is the force acting on the species of mass m, $C(f)$ is a collision operator describing the collisional evolution of f, and the subscripts $i = \{x, y, z\}$ indicate Einstein summation notation. By taking velocity moments of this equation assuming no applied forces ($F_i = 0$) and notably making no assumptions about the form of f, we obtain the following transport equations of the fluid moments:

$$\frac{\partial}{\partial t}\rho + \frac{\partial}{\partial x_i}\left(\rho u_i\right) = C^{(0)}, \tag{2}$$

$$\frac{\partial}{\partial t}\left(\rho u_i\right) + \frac{\partial}{\partial x_j}\left(\rho u_i u_j + p_{ij}\right) = C_i^{(1)}, \tag{3}$$

$$\frac{\partial}{\partial t}\left(\rho u_i u_j + p_{ij}\right) + \frac{\partial}{\partial x_k}\left(u_k[\rho u_i u_j + p_{ij}] + u_i p_{jk} + u_j p_{ik} + q_{ijk}\right) = C_{ij}^{(2)}, \tag{4}$$

where $C^{(0)}$, $C_i^{(1)}$ and $C_{ij}^{(2)}$ are the zeroth, first and second moments of the collision operator, respectively; the density and bulk velocity are defined as

$$\rho \equiv m \int f d^3\mathbf{v}, \qquad u_i \equiv \frac{m}{\rho} \int v_i f d^3\mathbf{v}, \tag{5}$$

and the pressure and heat flux as

$$p_{ij} \equiv m \int w_i w_j f d^3\mathbf{v}, \qquad q_{ijk} \equiv m \int w_i w_j w_k f d^3\mathbf{v}, \tag{6}$$

using the peculiar velocity $w_i = v_i - u_i$. The so-called *conservative* equations (Eqns. (2)–(4)) can be written succinctly in block-vector form as

$$\frac{\partial \mathbf{U}}{\partial t} + \frac{\partial \mathbf{F}_i}{\partial x_i} = \mathbf{S}, \tag{7}$$

where $\mathbf{U}$ is the vector of conservative variables, $\mathbf{F}_i$ is the vector of conservative fluxes in the i direction, and $\mathbf{S}$ is the vector of conservative sources, only self-collisions in this study. Typically, the quantities $\mathbf{U} = \{\rho, \rho u_i, \rho u_i u_i + p_{ii}\}$ are called conservative because they directly correspond to conservation of mass, momentum, and energy throughout the system, which results in a 5-moment system. This concept is generalized to the 10-moment system with the variables $\mathbf{U} = \{\rho, \rho u_i, \rho u_i u_j + p_{ij}\}$ even though, strictly speaking, the elements of the total stress tensor, $\rho u_i u_j + p_{ij}$, are not individually conserved through collisions. The full set of conservative 10-moment equations are exact up to conservation of mass and momentum, as the anisotropic pressure terms are solved for. This is an increase in fidelity over the perturbative closures used in the Navier-Stokes equations which use gradient-based approximations for the anisotropic pressure terms, while both the 10-moment and Navier-Stokes equations need closure for the heat flux.

On the other hand, the *primitive* variables can be defined as $\mathbf{\Pi} = \{\rho, u_i, p_{ij}\}$. The conservative equations can be re-written in primitive form, through a change of variables, as

$$\frac{D\rho}{Dt} + \rho \frac{\partial u_i}{\partial x_i} = \mathbb{c}^{(0)}, \tag{8}$$

$$\frac{Du_i}{Dt} + \frac{1}{\rho} \frac{\partial p_{ij}}{\partial x_j} = \mathbb{c}_i^{(1)}, \tag{9}$$

$$\frac{Dp_{ij}}{Dt} + \left(p_{ij} \frac{\partial u_k}{\partial x_k} + p_{ik} \frac{\partial u_j}{\partial x_k} + p_{jk} \frac{\partial u_i}{\partial x_k} + \frac{\partial q_{ijk}}{\partial x_k} \right) = \mathbb{c}_{ij}^{(2)}, \tag{10}$$

where $\frac{D}{Dt} = \frac{\partial}{\partial t} + u_i \frac{\partial}{\partial x_i}$ denotes the material derivative, and the primitive sources can be derived to be

$$\mathbb{c}^{(0)} = C^{(0)}, \tag{11}$$

$$\mathbb{c}_i^{(1)} = \frac{1}{\rho} \left(C_i^{(1)} - u_i C^{(0)} \right), \tag{12}$$

$$\mathbb{c}_{ij}^{(2)} = C_{ij}^{(2)} - u_i C_j^{(1)} - u_j C_i^{(1)} + u_i u_j C^{(0)}. \tag{13}$$

This form of the equations is useful because external forces, e.g., gravity, can accelerate the fluid but not increase the pressure (internal energy). For instance, if the z direction is aligned with gravitational acceleration, $C_z^{(1)} = \rho g$. If no source or sink exists in the mass conservation equation, $C^{(0)} = 0$. Thus, $\mathbb{c}_z^{(1)} = g$, which is a nonzero source term in the primitive equations. In addition, the force results in nonzero work from bulk acceleration: $C_{iz}^{(2)} = C_z^{(1)}(u_i + u_z \delta_{iz})$. However, $\mathbb{c}_{iz}^{(2)} = 0$ since the acceleration does not affect the internal energy p_{ij}. In this case, due to the transformation between primitive and conservative variables, a numerical solution of the conservative form of the 10-moment equations with sources may incur more numerical error than a solution with the primitive form.

The primitive equations, Eqns. (8)–(10), are written in block-vector form as

$$\frac{\partial \mathbf{\Pi}}{\partial t} + \mathbf{A}_i \frac{\partial \mathbf{\Pi}}{\partial x_i} = \mathbf{\Sigma}, \tag{14}$$

where $\mathbf{A}_i$ is the matrix for the fluxes transformed under a change-of-basis to the primitive variables, and $\mathbf{\Sigma}$ is the vector of primitive sources in Eqns. (11)–(13). See Appendix A for the derivation of the form of the matrix $\mathbf{A}_i$.

An eigenvalue analysis of the 10-moment system in the x direction, e.g., from A_x, is presented and discussed in Appendix A [40]. The analysis reveals that the system admits 10 waves which propagate at five different characteristic velocities:

$$\lambda_{1,2,3,4} = u_x, \tag{15}$$

$$\lambda_{5,7} = u_x + \sqrt{p_{xx}/\rho}, \qquad \lambda_{6,8} = u_x - \sqrt{p_{xx}/\rho}, \tag{16}$$

$$\lambda_9 = u_x + \sqrt{3p_{xx}/\rho}, \qquad \lambda_{10} = u_x - \sqrt{3p_{xx}/\rho}. \tag{17}$$

The characteristic velocities in the y and z directions have similar forms with the diagonal pressure element in that direction instead of p_{xx}. λ_{1-4} describe waves which travel with the fluid bulk velocity; they encompass an entropy wave associated with ρ,

and convective waves associated with transverse pressures p_{yy}, p_{yz}, and p_{zz}, which do not directly couple in the x direction. λ_{5-8} describe *slow* shear waves, which transport transverse information in the x direction; they encompass waves associated with v, w, p_{xy}, and p_{xz}. Note that these waves do not affect the longitudinal pressure, but they are advected up- and down-stream at a thermal speed. Finally, $\lambda_{9,10}$ are the *fast* acoustic waves which affects all primitive variables and are associated with u, and p_{xx}; they carry information about the longitudinal velocity (i.e., v_x and v_x^2) being transported in the x direction and move at the fastest wavespeed. In the collisional limit, the 10-moment acoustic waves reduce to the classical Euler acoustic waves of speed $\sqrt{5p/3\rho}$, while the shear waves associated with off-diagonal pressures vanish [40]. Qualitatively, the Euler acoustic waves can be thought of as the 10-moment acoustic wave for p_{xx} moving at $u \pm \sqrt{3p_{xx}/\rho}$ being slowed because the wave needs to also excite the transverse on-diagonal pressures, which travel more slowly. It is important to note that under all physically permissible conditions, $\{\rho, p_{xx}, p_{yy}, p_{zz}\} > 0$, so the wavespeeds are necessarily real and finite-valued and thus the inviscid portion of the 10-moment system is hyperbolic. This is particularly important for numerical solution of these equations, which will be described in Section 2.3.

2.2. Collision operator: ellipsoidal-statistical BGK model

A key measure in the validity of the fluid continuum approximation is the Knudsen number, $\mathrm{Kn} = \lambda_{\mathrm{MFP}}/L$, where λ_{MFP} is the particle mean free path and L is a characteristic physical length scale. For small Kn, particles experience many collisions as they traverse the relevant domain, and so they can be considered to be in equilibrium with one another, thus warranting an equilibrium fluid formulation. For large values of Kn, particles may not equilibrate between one another and assumptions about near-Maxwellian VDFs must be relaxed. Thus, an accurate collision operator is key to the implementation of fluid models.

A 5-moment system that uses a gradient-based closure (e.g., Navier-Stokes equations) is typically valid for Knudsen number $\mathrm{Kn} \ll 1$, resulting in a small deviation of the VDFs from the equilibrium Maxwellian VDF. Because the 10-moment system evolves the anisotropic pressure, it is expected that it can more accurately capture non-Maxwellian flows. While the 10-moment system is exact up to the anisotropic pressure, the heat flux, which corresponds to the third moment of the VDF, must be closed. In addition, the collisional terms must be defined. The Boltzmann operator, which is valid for binary, elastic collisions, is given by

$$C_B(f_1, f_2) = \iint g(f_1' f_2' - f_1 f_2)\sigma d\Omega d^3\mathbf{v}_2, \tag{18}$$

where f' is the post-collision distribution function, subscripts 1 and 2 denote two different particles, $g = |\mathbf{v}_2 - \mathbf{v}_1|$ is the magnitude of the relative velocity, σ is the collision cross section, and $d\Omega$ is the differential solid angle of the deflected particle. In general, this collision integral is difficult to evaluate but under certain assumptions, it can be evaluated using the theory by Chapman and Cowling [7,41]. Recent work in plasma simulations has evaluated this integral in the calculation of collision frequencies of the various interactions extant in plasmas [42]. Constructing the closure model considering a Boltzmann operator is reported in References [7] and [43] and will be reserved for future work. Instead, we employ the Bhatnagar-Gross-Krook (BGK) operator [10]

$$C(f) = \frac{1}{\tau}\left(f^{\mathrm{relax}} - f\right), \tag{19}$$

where τ is the characteristic relaxation time, and f^{relax} is the relaxation VDF that the non-Maxwellian f locally relaxes towards through collisions. The BGK operator is a mathematical simplification that does not physically capture the particle kinetics but is designed to conserve mass, momentum, and energy. It is typically taken that $f^{\mathrm{relax}} = f^M$ is the equilibrium Maxwellian distribution:

$$f^{\mathrm{relax}} = f^M \equiv \frac{\rho}{m}\left(\frac{\rho}{2\pi p}\right)^{3/2} \exp\left(-\frac{\rho}{2p}\mathbf{w}^2\right), \tag{20}$$

where $p = p_{ii}/3$ is the isotropic pressure and $p = \rho RT = nk_BT$ (here $R = k_B/m$ is the specific gas constant, $n = \rho/m$ is the number density, k_B is the Boltzmann constant, and T is the isotropic temperature). The model describes the relaxation of the distribution function towards equilibrium with characteristic time τ. The characteristic time is chosen so that in the continuum limit, the correct coefficient of viscosity $\mu = \tau p$ is predicted. This model weakly satisfies Boltzmann's H-theorem and correctly predicts the fluid behavior in the two limits. (1) $\tau \to 0$: infinitely collisional and immediate relaxation to Maxwellian and (2) $\tau \to \infty$: collisionless and thus no effect of the collision operator. A significant limitation of the BGK model, however, is that it incorrectly predicts a Prandtl number $\mathrm{Pr} = c_p\mu/\kappa = 1$, where c_p is the specific heat at constant pressure and κ is the coefficient of thermal conductivity. This value of the Prandtl number is in contrast to the results from the Boltzmann operator and experimental evidence, both of which show Pr closer to 2/3.

Another approximate collision term proposed by Holway [11] is the ellipsoidal-statistical BGK (ES-BGK) operator, which preserves the simple form of the BGK model but allows for setting a physically consistent $\mathrm{Pr} \neq 1$. The relaxation VDF is considered to be an ellipsoidal distribution function:

$$f^{\mathrm{relax}} = f^{ES} \equiv \frac{\rho}{m}\left[\frac{\rho^3}{(2\pi)^3\,|\wp|}\right]^{1/2} \exp\left(-\frac{\rho}{2}w_i\wp_{ij}^{-1}w_j\right), \tag{21}$$

where $|\wp|$ and $\wp^{-1}$ are the determinant and the inverse, respectively of a pressure tensor $\wp$, defined as

$$\wp_{ij} = (1-\eta)p\delta_{ij} + \eta p_{ij}, \tag{22}$$

and η is a free parameter. This form of the modified relaxation VDF retains conservation of mass, momentum, and energy, but allows one to achieve a physically consistent Prandtl number, $\mathrm{Pr} = (1-\eta)^{-1}$ by tuning η [11,44]. A derivation of this relationship for the 10-moment model is presented in the next section.

2.3. Closure

The equations for conservation of mass and momentum, Eqns. (2)–(3), are exact in that no assumptions have been made on any of the variables, unlike Navier-Stokes-like equations where assumptions are made on the form of shear stress, which comes from an anisotropic pressure tensor. The remaining six equations for the full pressure tensor (note: $p_{ij} = p_{ji}$), Eqn. (4), would also be exact if the form of the collisions, C, and heat flux, q_{ijk}, are known. A higher fidelity option is to take the third order moment of the kinetic transport equation so that the heat flux tensor is modeled directly, adding ten more equations to the 10-moment system. However, even if the heat flux equation is solved, the closure of the heat flux equation, i.e., closure for the fourth moment would still remain a question [45]. Another option is to consider the contracted heat flux q_{ikk}, which adds three equations into the 10-moment system, making it a 13-moment system [42]. The further addition of a contracted fourth moment, r_{iijj}, yields the 14-moment system that is often used for maximum-entropy formulations [12,46]. However, while taking higher order moments may capture the physics with higher fidelity, the key limitation is that the inviscid portion of the system may lose strict hyperbolicity, i.e., in general, the system can admit singular and imaginary wave speeds. Furthermore, as mentioned above, Junk proved that above the 10-moment system, there are certain sets of fluid moments, i.e., $\{\rho, u_i, p_{ij}, q_{ijk}, \text{etc.}\}$, for which there is no suitable definition for a maximum-entropy distribution, or in other words, there are distribution functions with negative probability densities or singular coefficients that have lower entropy than any physically suitable distribution function [32,33].

2.3.1. Chapman-Enskog expansion

In this study, the 10-moment system is chosen as a step to expand the capability of Navier-Stokes (5-moment) solvers for systems farther from equilibrium, i.e., incorporating higher Knudsen number effects. The model no longer requires explicit description of the viscosity, but still requires closure for the heat flux (third moment). There are various ways to perform the closure; one can expand about a Maxwellian VDFs or other equilibrium distributions in terms of polynomials or spherical harmonics [23,31,47,48]. As an ansatz, we will perform a Chapman-Enskog type closure, which is an expansion in terms of the Knudsen number, using the 10-moment equations and assuming perturbation about an *isotropic* Maxwellian distribution following a similar derivation in Ref. [1]. The key hypothesis is that the unperturbed distribution function should be a Maxwellian to satisfy the Boltzmann H-theorem. This assumption is not trivial, as previous work has been done performing a perturbation around a Gaussian distribution [31,46], a discussion of which is presented in Section 4.2.2.

We begin by nondimensionalizing Eqn. (1) using the ES-BGK operator as shown in Eqn. (19),

$$\xi\left(\frac{\partial}{\partial\hat{t}}\hat{f} + \hat{v}_i\frac{\partial}{\partial\hat{x}_i}\hat{f} + \hat{F}_i\frac{\partial}{\partial\hat{v}_i}\hat{f}\right) = \frac{1}{\hat{\tau}}\left(\hat{f}^{ES} - \hat{f}\right), \tag{23}$$

where reference values for length, velocity and relaxation time are used for nondimensionalized parameters as follows,

$$\hat{f} \equiv f/\left(v_{\mathrm{ref}}^{-3}n_{\mathrm{ref}}\right), \quad \hat{x} \equiv x/L_{\mathrm{ref}}, \quad \hat{v} \equiv v/v_{\mathrm{ref}}, \quad \hat{t} \equiv t/\left(v_{\mathrm{ref}}^{-1}L_{\mathrm{ref}}\right), \quad \hat{F} \equiv F/\left(mv_{\mathrm{ref}}^{2}L_{\mathrm{ref}}^{-1}\right), \quad \hat{\tau} \equiv \tau/\tau_{\mathrm{ref}}, \tag{24}$$

and ξ is a smallness parameter:

$$\xi = \frac{v_{\mathrm{ref}}\tau_{\mathrm{ref}}}{L_{\mathrm{ref}}}. \tag{25}$$

Here, ξ is similar to the Knudsen number when $v_{\mathrm{ref}}\tau_{\mathrm{ref}}$ is chosen to equal the mean free path. Thus, under the assumption that f can be expressed as a perturbation about a Maxwellian, we may write

$$\hat{f} = \hat{f}^M\left(1 + \xi\phi_1 + \xi^2\phi_2 + \ldots\right), \tag{26}$$

where ϕ_n is the n^{th} order perturbation function. Substituting Eqn. (26) into Eqn. (23) with no external forces, and only retaining terms to first order in ξ, we can arrive at equation for the first-order perturbation

$$\xi\left(\frac{\partial}{\partial\hat{t}}\hat{f}^M + \hat{v}_i\frac{\partial}{\partial\hat{x}_i}\hat{f}^M\right) = \frac{1}{\hat{\tau}}\left(\hat{f}^{ES} - \hat{f}^M - \hat{f}^M\xi\phi_1\right). \tag{27}$$

It is to be noted that the collisional equilibrium distribution, f^{ES}, and the leading-order unperturbed distribution, f^M, do not cancel out exactly, and the factor of ξ cannot be cancelled out. The ES-BGK approach is used to derived 5-moment Navier-Stokes system in Ref. [49].

To eliminate the derivatives of f^M from Eqn. (27), we note that f^M, as shown in Eqn. (20), is a function of only ρ, u_i, and p, and the derivatives of f^M can be written, using the chain rule, in terms of derivatives of the primitive quantities:

$$\frac{\partial}{\partial\zeta}f^M = \frac{\partial f^M}{\partial\rho}\frac{\partial\rho}{\partial\zeta} + \frac{\partial f^M}{\partial u_i}\frac{\partial u_i}{\partial\zeta} + \frac{\partial f^M}{\partial p}\frac{\partial p}{\partial\zeta}, \tag{28}$$

where $\zeta = t, x_i$. Rearranging Eqns. (2)–(4) to isolate the temporal derivatives of the primitive variables $\{\rho, u_i, p = p_{ii}/3\}$ and dropping the second-order dependence on q_{ijk} yields

$$\frac{\partial \rho}{\partial t} = -\rho \frac{\partial u_i}{\partial x_i} - u_i \frac{\partial \rho}{\partial x_i}, \tag{29}$$

$$\frac{\partial u_i}{\partial t} = -\frac{1}{\rho} \frac{\partial p_{ij}}{\partial x_j} - u_j \frac{\partial u_i}{\partial x_j}, \tag{30}$$

$$\frac{\partial p}{\partial t} = -\frac{2}{3} p_{ij} \frac{\partial u_i}{\partial x_j} - p \frac{\partial u_i}{\partial x_i} - u_i \frac{\partial p}{\partial x_i}. \tag{31}$$

Note that we only require the time derivative of p, not p_{ij}, but it is expressed in terms of the full pressure tensor p_{ij}. Using Eqns. (28)–(31) in Eqn. (27), yields after redimensionalization:

$$\xi \phi_1 f^M = -\tau f^M \left[\left(\frac{\rho w_i w_j}{p} - \frac{p_{ij}}{p} \frac{\rho w^2}{3p} + \frac{p_{ij}}{p} - \delta_{ij} \right) \frac{\partial u_i}{\partial x_j} + w_j \left(\frac{\rho w^2}{2p} - \frac{5}{2} \right) \frac{\partial}{\partial x_j} \ln \left(\frac{p}{\rho} \right) \right] + \left(f^{ES} - f^M \right). \tag{32}$$

The canonical Chapman-Enskog [1] perturbation can be recovered under substitution of $f^{ES} \to f^M$ and $p_{ij} \to p\delta_{ij}$ in Eqn. (32). The additional pressure-tensor dependent terms correspond to anisotropy in the viscosity tensor. It is to be noted that this closure remains a first-order perturbative closure around a Maxwellian, and thus the assumptions on the smallness of ξ break down when considering strongly non-equilibrium flows. As mentioned above, a general closure for high Knudsen number ($\mathrm{Kn} \gtrsim 0.1$) would require treatment of nonlocal transport; however, the present study will focus on demonstrating the efficacy of the Maxwellian closure in Eqn. (32) despite this caveat.

2.3.2. Heat flux tensor

Using the first-order approximation of $f \simeq f^M \left(1 + \xi \phi_1\right)$, where ϕ_1 is as in Eqn. (32), the heat flux can be calculated by taking the third central velocity moment:

$$q_{ijk} = -\tau p \left[\delta_{ij} \frac{\partial}{\partial x_k} \left(\frac{p}{\rho} \right) + \delta_{ik} \frac{\partial}{\partial x_j} \left(\frac{p}{\rho} \right) + \delta_{jk} \frac{\partial}{\partial x_i} \left(\frac{p}{\rho} \right) \right]. \tag{33}$$

It is to be noted that the third central moment vanishes for both f^{ES} (Eqn. (21)) and f^M (Eqn. (20)), and furthermore that the first gradient based-term, i.e., $\frac{\partial u_i}{\partial x_j}$, in Eqn. (32) is an even function of w. Thus, the contribution to the third-moment heat flux is only from the second gradient-based term, i.e., $\frac{\partial}{\partial x_j} \ln(p/\rho)$, as shown in Eqn. (33). The form of the heat flux is parabolic in nature, which may seem contrary to the convenient mathematical properties of purely hyperbolic systems, i.e., characteristic curves and a solution describable purely through propagation of waves of finite speed. The parabolic term effectively introduces an infinitely large wavespeed (cf. parabolic PDEs). However, while purely hyperbolic systems of equations have many advantages, having limited finite (real) wavespeeds may not be suitable to capturing all of the particle dynamics. Particularly for fluids, there would inevitably be high-energy particles in the tails of distributions with speeds greater than the maximum wavespeed of the set of PDEs (cf. speed of sound). Hence, parabolic source terms may allow for the capture of effects not describable by purely hyperbolic systems. Care must be taken, however, that the closed system of equations does not admit unstable wavenumbers or infinite spatial wavespeeds; a complete dispersion analysis of the closed 10-moment equations is reserved for future work.

2.3.3. Prandtl number

While the heat flux tensor obtained in Eqn. (33) can be directly applied in the 10-moment system, the Prandtl number is obtained by taking the ratio of the 5-moment heat flux and viscosity. Using Eqn. (33), the contracted heat flux can be obtained as

$$q_i = \left\langle \frac{w^2}{2} w_i \right\rangle = \frac{1}{2} q_{ikk} = -\kappa \frac{\partial T}{\partial x_i}, \tag{34}$$

where

$$\kappa = \frac{5\tau}{2} \frac{p k_B}{m} \tag{35}$$

is known as the thermal conductivity.

While the anisotropic pressure tensor is solved for directly in the 10-moment model (Eqn. (4)), we would like to compare the results from the Chapman-Enskog expansion to a Navier-Stokes formulation to determine an effective Prandtl number. The second central velocity moment (i.e., Eqn. (6)) can be derived using Eqn. (32) as

$$p_{ij} = (1 - \eta) p \delta_{ij} + \eta p_{ij} - t_{ij}, \tag{36}$$

where η is the free parameter in the ES-BGK model (Eqn. (22)) and t_{ij} is the deviatoric stress tensor that appears in the Navier-Stokes equations:

$$t_{ij} = \tau p \left(\frac{\partial u_i}{\partial x_j} + \frac{\partial u_j}{\partial x_i} - \frac{2}{3} \frac{\partial u_k}{\partial x_k} \delta_{ij} \right). \tag{37}$$

Upon rearranging, one obtains that

$$p_{ij} - p\delta_{ij} = -\frac{\tau p}{1-\eta} \left(\frac{\partial u_i}{\partial x_j} + \frac{\partial u_j}{\partial x_i} - \frac{2}{3} \frac{\partial u_k}{\partial x_k} \delta_{ij} \right). \tag{38}$$

Therefore, the use of the ES-BGK model has effectively reduced the coefficient of viscosity, $\mu = \tau p$, by a factor of $(1-\eta)$, while the heat flux is not affected by η. Thus, the Prandtl number for the ES-BGK closure of monatomic gases can be written as

$$\mathrm{Pr} = \frac{c_p \mu}{\kappa} = \left(\frac{5k_B}{2m} \right) \left(\frac{\tau p}{1-\eta} \right) \left(\frac{5\tau p k_B}{2m} \right)^{-1} = \frac{1}{1-\eta}, \tag{39}$$

where $c_p = 5k_B/2m$ and $\gamma = 5/3$ for an ideal monatomic gas. This illustrates the utility of the ES-BGK operator. As mentioned above, for the conventional BGK, i.e., $\eta = 0$, the predicted Prandtl number becomes 1, which is not physically representative; many gases, particularly monatomic gases, have $\mathrm{Pr} \simeq 2/3$. This Prandtl number is also observed in DSMC simulations using hard sphere collisions as shown/discussed in Refs. [50] and [51]. We emphasize that the ES-BGK model is a mathematical simplification compared to the closure assuming the Boltzmann operator. While there are (past and ongoing) studies that propose the Boltzmann closure for intraspecies and interspecies collisions [42], the goal of this paper is to demonstrate the 10-moment system with the heat flux closure model by benchmarking against 5-moment (Navier-Stokes) and kinetic (DSMC) results. Derivation and implementation of higher fidelity closure models (e.g., Boltzmann collision operator [42]) and the closure for different types of collisional processes (e.g., intermolecular and Coulomb collisions) are reserved for future work.

2.3.4. Collisional transfer terms

For the purpose of benchmarking, in this paper, we have chosen $\mathrm{Pr} = 2/3$, i.e., $\eta = -1/2$, for the collisional closure in the 10-moment model for consistency with the DSMC results for monatomic gases. The pressure tensor of the associated equilibrium distribution, Eqn. (22), is

$$\wp_{ij} \left(\mathrm{Pr} = \frac{2}{3} \right) = \frac{3}{2} p\delta_{ij} - \frac{1}{2} p_{ij}. \tag{40}$$

Comparing this to the Maxwellian pressure tensor, Eqn. (20) with $\wp_{ij}(\mathrm{Pr}=1) = p_{ij}^M = p\delta_{ij}$, it is seen that the ES-BGK model weighs the isotropic pressure in the collision operator more than in the BGK model. As f^{ES} is designed to have the same zeroth and first moments as f, the moments of the ES-BGK collision operator yield

$$C_{\mathrm{ES}}^{(0)} = 0 \tag{41}$$

$$C_{\mathrm{ES},i}^{(1)} = 0 \tag{42}$$

$$C_{\mathrm{ES},ij}^{(2)} = \frac{1}{\tau} \left(\wp_{ij} - p_{ij} \right) = \frac{1}{\tau} \left(\left[(1-\eta) p\delta_{ij} + \eta p_{ij} \right] - p_{ij} \right) = \frac{1-\eta}{\tau} \left(p\delta_{ij} - p_{ij} \right) = \frac{1}{\mathrm{Pr}} \frac{p\delta_{ij} - p_{ij}}{\tau}. \tag{43}$$

As can be seen from Eqn. (43), $\mathrm{Pr} = 2/3$ results in a faster equilibration (i.e., smaller effective τ) as compared to the $\mathrm{Pr} = 1$ case. While the BGK operator is a mathematical simplification of the Boltzmann operator, setting $\mathrm{Pr} = 2/3$ in the 10-moment closure results in better agreement between 10-moment and kinetic results than $\mathrm{Pr} = 1$.

The canonical 5-moment equations are recovered in the limit of $\tau \to 0$, which immediately damps any anisotropy and relaxes the non-equilibrium distribution to an equilibrium Maxwellian.

2.4. Relaxation time

For the 10-moment model, the characteristic relaxation time τ must be assigned as introduced in Eqn. (19) and shown in Eqn. (43). While a constant τ throughout the domain is mathematically simple, elastic binary intra-species collisions are dependent on the local temperature and density (or pressure). From classical kinetic theory [1], the mean free path for like-particle collisions in an ideal gas is given by

$$\lambda_{\mathrm{MFP}} = \frac{1}{\sqrt{2}\pi d^2 n}, \tag{44}$$

where d is the kinetic diameter of a particle. Then, the collision frequency can be approximated as

$$\nu \simeq \frac{\langle v \rangle}{\lambda_{\mathrm{MFP}}} \propto n\sqrt{T} \propto \sqrt{np}, \tag{45}$$

where $\langle v \rangle$ is the particle average speed and the ideal gas equation of state is assumed. Considering that the characteristic relaxation time of the VDFs is proportional to the characteristic time for collisional events, i.e., $\tau \propto \nu^{-1}$, the characteristic time can be written as

$$\frac{\tau}{\tau_0} = \left(\frac{n}{n_0}\right)^{-0.5} \left(\frac{p}{p_0}\right)^{-0.5}, \tag{46}$$

where n_0 and p_0 are problem-dependent reference values for number density and pressure and τ_0 is a free parameter used to vary the characteristic relaxation time. The choice of τ_0 for consistency with kinetic simulations is discussed in Section 2.5.

2.5. Direct Simulation Monte Carlo

To assess the ability of the 10-moment model to capture finite kinetic effects compared to the 5-moment system, we make a comparison of the fluid models to the kinetic transport equation whose approximate solution can be obtained from the DSMC simulations of a monatomic gas. Here, we consider argon ($\gamma = 5/3$, $m = 40$ amu). The DSMC simulations in 1-D are performed as outlined in Ref. [51] using the No-Time-Counter (NTC) methods of Bird [52]. We employ the variable hard-sphere model to capture the known dependence of the collisional cross-section on the relative speed of particles:

$$d = d_r \left(\frac{g_r}{g}\right)^{\omega}, \tag{47}$$

where d is the particle diameter, d_r is a reference diameter, g is the relative speed between particles, g_r is a reference speed, and ω is the power-law exponent. As shown in Ref. [51], the reference speed is determined as

$$g_r^2 = \frac{2k_B T_r}{m} \left[\Gamma(2-\omega)\right]^{-1/\omega}, \tag{48}$$

where T_r is a reference temperature and $\Gamma(x)$ is the Gamma function. The power-law exponent $\omega = 0.2$ is chosen in accordance with its good agreement to the experimental data of normal shock profiles of Alsmeyer [51,53].

To benchmark the 10-moment fluid model with the kinetic results, we need to define the reference diameter in such a way that is consistent with the characteristic relaxation time of the fluid, as used in Eqns. (19) and (46). Using the results of Chapman-Enskog theory with a BGK operator [1], the characteristic relaxation time in DSMC can be written as

$$\tau_{\mathrm{DSMC}} = \frac{\mu}{p} = \sqrt{\frac{2\rho}{\pi p}} \lambda_{\mathrm{MFP}} = \sqrt{\frac{2\rho}{\pi p}} \frac{m}{\sqrt{2}\rho\pi d_r^2} = \frac{m}{\pi^{3/2} d_r^2} (\rho p)^{-1/2} = \frac{\sqrt{m}}{\pi^{3/2} d_r^2} (np)^{-1/2}, \tag{49}$$

which directly corresponds to the scaling law in Eqn. (46). We want the DSMC and fluid models to have the same initial condition, i.e., m, $\rho(x, t=0)$, $u_i(x, t=0)$, and $p_{ij}(x, t=0)$; while $\tau_{0,\mathrm{fluid}}$ is a fully independent free parameter and $\tau_{0,\mathrm{DSMC}}$ is dependent on the reference diameter. Because the heat flux is the only term requiring closure in the 10-moment model, the values of $\tau_{0,\mathrm{fluid}}$ and $\tau_{0,\mathrm{DSMC}}$ are chosen so that the estimates of the heat flux from the kinetic and fluid Chapman-Enskog theory are consistent. Thus, we seek to find a definition of the reference diameter d_r that provides the same form of the thermal conductivity κ between the DSMC and 10-moment models.

It can be deduced from Eqn. (49) that

$$\tau_{\mathrm{DSMC}} = \frac{\mathrm{Pr}\, \kappa_{\mathrm{DSMC}}}{c_p p}, \tag{50}$$

and thus by definition, the thermal conductivity for DSMC can be written as

$$\kappa_{\mathrm{DSMC}} = \frac{5\tau_{\mathrm{DSMC}}}{2\mathrm{Pr}} \frac{p k_B}{m}. \tag{51}$$

By comparison with Eqn. (35), Eqn. (51) implies that

$$\tau = \tau_{\mathrm{DSMC}} \frac{1}{\mathrm{Pr}}. \tag{52}$$

This discrepancy is solely from the fact that the fluid equation is using the ES-BGK operator. Therefore, for DSMC simulations to be consistent with the 10-moment fluid model, the reference diameter in the DSMC is chosen as

$$d_r^2 = \frac{m}{\rho\pi\tau_{\mathrm{DSMC}}} \sqrt{\frac{\rho}{\pi p}} = \frac{m}{\rho\pi\left(\mathrm{Pr}\ \tau_{\mathrm{fluid}}\right)} \sqrt{\frac{\rho}{\pi p}}, \tag{53}$$

or, substituting in with Eqn. (46),

$$d_r^2 = \frac{m}{\rho_0\pi\left(\mathrm{Pr}\ \tau_{0,\mathrm{fluid}}\right)} \sqrt{\frac{\rho_0}{\pi p_0}}, \tag{54}$$

where the reference values are taken to be the same as the fluid model.

2.6. 5-moment system

The 10-moment results are compared with DSMC (kinetic) to show how much non-Maxwellian effects the 10-moment system can capture. Simultaneously, we compare the 10-moment results with 5-moment systems, including Navier-Stokes and Euler, illustrating that the 10-moment system asymptotes to the 5-moment system in the limit of linear perturbation of the non-Maxwellian VDF.

2.6.1. Navier-Stokes equations

From the 10-moment equation system, the Navier-Stokes equations can be derived under two main assumptions. First, the anisotropic pressure is divided into the isotropic pressure and an approximate shear stress, i.e., $p_{ij} \rightarrow p\delta_{ij} - t_{ij}$ so that

$$\frac{\partial}{\partial t}\left(\rho u_i\right) + \frac{\partial}{\partial x_j}\left(\rho u_i u_j + p\delta_{ij} - t_{ij}\right) = C_i^{(1)}, \tag{55}$$

where the collisional drag $C_i^{(1)} = 0$ for self-collisions. The approximate shear stress tensor, t_{ij} can be obtained from the Chapman-Enskog expansion in the limit of isotropic pressure [1]:

$$t_{ij} = \mu\left(\frac{\partial u_i}{\partial x_j} + \frac{\partial u_j}{\partial x_i} - \frac{2}{3}\frac{\partial u_k}{\partial x_k}\delta_{ij}\right), \tag{56}$$

where the coefficient of viscosity, $\mu = \tau p$ and the collision frequency is also calculated using Eqn. (46). In addition, the conservation of energy can be written as

$$\frac{\partial}{\partial t}\left(\rho E\right) + \frac{\partial}{\partial x_i}\left[\rho u_i E + u_j\left(p\delta_{ij} - t_{ij}\right) + q_i\right] = C^{(2)} = \frac{1}{2}C_{ii}^{(2)}, \tag{57}$$

where $\rho E = (3p + \rho u_i u_i)/2$ is the total energy density and $C^{(2)}$ is the net volumetric energy input, which vanishes for purely elastic intraspecies collisions, as there is no energy exchange between the system and the surroundings. A more sophisticated treatment of the Navier-Stokes closure using the Boltzmann collision operator has been done in previous work and yields the physically accurate value for the Prandtl number of 2/3 [51]. To provide the highest-fidelity comparison for the 10-moment results, we employ Navier-Stokes equations using the Boltzmann collision operator. While this choice may allow for a discrepancy between the Navier-Stokes and 10-moment solutions due to the different form of the collisional closure, it allows for the most robust demonstration of the merits of the 10-moment model. The Navier-Stokes heat flux is then given as,

$$\frac{1}{2}q_{ikk} \simeq q_i = -\frac{15}{4}\tau p\frac{\partial}{\partial x_i}\left(\frac{p}{\rho}\right). \tag{58}$$

2.6.2. Euler equations

The 5-moment Euler system is equivalent to the Navier-Stokes system in the limit of $\tau \rightarrow 0$. Namely, there are no deviatoric stresses or heat flux and thus has no closure. This model takes the form of a purely hyperbolic set of transport equations for mass, momentum, and energy, i.e., $\{\rho, \rho u_i, \rho E\}$, with no sources.

3. Numerical methods

The fluid equations, as shown in Eqns. (2)–(4), are numerically integrated forward in time explicitly using a finite-volume approach. By solving for flux of the conservative variables between volume elements, we can ensure that mass, momentum, and energy are conserved. However, the sources act directly on the primitive variables, corresponding to an isotropization of p_{ij}, *not* $p_{ij} + \rho u_i u_j$; therefore, it is logical that the source update should be performed directly on the primitive variables so as to avoid numerical errors between converting between primitive and conservative variables.

3.1. Time-stepping

Second-order Strang splitting is employed, wherein primitive variables are updated a half-timestep using only the sources, then the conservative variables are updated a full timestep using only the fluxes, then finally the primitive variables are updated the last half timestep using the sources again. For increased accuracy and to reduce spurious oscillations, each timestep is taken using the third-order strong stability-preserving Runge-Kutta (SSP-RK3) for stability [54,55]. Thus the advancement of the variables from timestep n to $n+1$ is shown in Eqn. (59):

$$\mathbf{\Pi}^n \xrightarrow[\text{Sources}]{\Delta t/2} \mathbf{\Pi}' \rightarrow \mathbf{U}' \xrightarrow[\text{Fluxes}]{\Delta t} \mathbf{U}'' \rightarrow \mathbf{\Pi}'' \xrightarrow[\text{Sources}]{\Delta t/2} \mathbf{\Pi}^{n+1}, \tag{59}$$

where Δt is the timestep and $\mathbf{\Pi}' \rightarrow \mathbf{U}'$ and $\mathbf{\Pi}'' \rightarrow \mathbf{U}''$ indicate transforming to the conservative variables from the primitive variables and vice versa, respectively. The discretized form of the source update of the primitive variables at cell index ℓ can be written as

$$\left(\frac{\mathbf{\Pi}'_\ell - \mathbf{\Pi}^n_\ell}{\Delta t/2}\right)_{\text{Sources}} = \mathbf{\Sigma}\left(\mathbf{\Pi}^n_\ell\right), \tag{60}$$

where $\mathbf{\Sigma}$ is the primitive source term shown in Eqn. (14). For neutral gases, where we only consider elastic collisions between like-particles, the source term for the anisotropic pressure contains relaxation to an isotropic Maxwellian:

$$\left(\frac{\partial}{\partial t}p_{ij,\ell}\right)_{\text{Sources}} = \frac{1}{\tau_\ell}\left(p_\ell \delta_{ij} - p_{ij,\ell}\right). \tag{61}$$

To perform the inviscid flux updates, we employ Steger-Warming inviscid flux vector splitting [56], for which the details of the eigendecomposition of the 10-moment system have been described in previous works [40] and are reproduced in Appendix A. The fact that the eigenvalues remain real and finite under all conditions means that the equations remain hyperbolic and thus can be solved through extensions of established numerical schemes for the inviscid fluxes of hyperbolic PDEs.

For one-dimensional problems, assuming equidistant cells where the cell size is Δx, the discretized form of the flux update of the conservative variables at cell index ℓ is given by

$$\left(\frac{\mathbf{U}''_\ell - \mathbf{U}'_\ell}{\Delta t}\right)_{\text{Fluxes}} + \frac{\mathbf{F}_{x,\ell+1/2} - \mathbf{F}_{x,\ell-1/2}}{\Delta x} = 0, \tag{62}$$

where $\mathbf{F}_x$ is the flux function at cell interfaces including the inviscid and viscous fluxes. Using flux vector splitting, the flux function in Eqn. (62) can be written as,

$$\mathbf{F}_x\left(x_{\ell+1/2}\right) = \mathbf{F}_x^+\left[\mathbf{U}^L\left(x_{\ell+1/2}\right)\right] + \mathbf{F}_x^-\left[\mathbf{U}^R\left(x_{\ell+1/2}\right)\right] + \mathbf{F}_{x,c}\left[\mathbf{U}^L, \mathbf{U}^R, \nabla\mathbf{U}\right], \tag{63}$$

where $\mathbf{F}_x^\pm$ are the rightward and leftward moving Steger-Warming fluxes, $\mathbf{U}^{L/R}$ are the states reconstructed using Monotonic Upwind Scheme for Conservation Laws (MUSCL) with the van Leer harmonic limiter [57] at the left (L) and right (R) sides of the interface at position $x_{\ell+1/2}$, and $\mathbf{F}_{x,c}$ is the viscous flux due to closure, i.e., q_{ijk} for 10-moment and t_{ij} and q_k for Navier-Stokes. The gradient values used to find q and t at cell interfaces are calculated using central differencing, i.e., $\left(\frac{\partial Q}{\partial x}\right)_{\ell+1/2} = \left(Q_{\ell+1} - Q_\ell\right)/\Delta x$. The values of τ and p at the interface in Eqns. (33), (56), and (58) are calculated using the average of $\mathbf{U}^L$ and $\mathbf{U}^R$.

Eqn. (62) is solved with the conservative variables at the cell centers, $\mathbf{U}_{\text{ctr}}$ being updated as

$$\frac{\partial \mathbf{U}_{\text{ctr}}}{\partial t} = -\sum_{\text{int}} \frac{\mathbf{F}_{\text{int}}}{A_{\text{ctr}}}, \tag{64}$$

where the sum is over all of the interfaces of the cell and A_{ctr} is the area of the cell. For two-dimensional problems, a zeroth order reconstruction is used such that the value within each cell is assumed to be constant. Likewise, the outward-moving Steger-Warming fluxes through each interface are calculated as

$$\mathbf{F}_{\text{int}} = \left[\mathbf{F}^+\left(\mathbf{U}^-\right) + \mathbf{F}^-\left(\mathbf{U}^+\right) + \mathbf{F}_c\left(\mathbf{U}, \nabla\mathbf{U}\right)\right]_i \mathbb{m}_i, \tag{65}$$

where $\mathbf{F}^\pm$ are the outward and inward moving Steger-Warming fluxes, $\mathbf{U}^\pm$ are the conservative quantities on the outside and inside of the interface, and $\mathbb{m}$ is the interface-length weighted normal vector of the interface. The gradients in the x and y directions are calculated at interfaces using the schematic shown in Fig. 1. We define auxiliary points along the lines between the cell center points, and interpolate the values on those auxiliary points from the cell center values. Then, both the x- and y-gradients can be calculated on all interfaces to find the gradient of the properties in the interface normal direction.

In addition, the timestep size Δt is taken to satisfy $\Delta t < \tau$ and the Courant–Friedrichs–Lewy (CFL) condition. In the present 10-moment model, non-oscillatory (stable) results are obtained for the CFL condition of

$$C = \frac{|\lambda_i|_{\max}\Delta t}{\Delta x_i} \leq 0.3, \tag{66}$$

where $|\lambda_i|_{\max}$ is the fastest wavespeed in the i direction, $|\lambda_i|_{\max} = |u_i| + \sqrt{3p_{ii}/\rho}$.

3.2. Boundary conditions

For one dimensional test cases (Sections 4 and 5), the 10-moment solver is compared with DSMC and Navier-Stokes solutions considering a 1-D shock tube. In these test cases, the initial condition consists of a discontinuity at the center of the domain, i.e., $x = 0$, and assumes that the states across the discontinuity are infinitely long and uniform. For these test cases, a Neumann boundary condition is used, whereby two ghost cells are added to the left and right sides of the domain for the fluid solvers, whose states are set equal to the last cell within the domain on either side, to obtain an unperturbed uniform distribution near the boundaries. These ghost cells are used when calculating the MUSCL-reconstructed states and thus the fluxes at the boundaries. Simulations with Dirichlet boundary conditions at the initial conditions sometimes led to a longer time to reach steady state as waves were reflected off the boundary and perturbed the structure in the domain. For cases reaching steady-state, the cells near the boundary were confirmed to be unperturbed from the initial conditions.

For the two-dimensional test case (Section 6), we propose an oblique shock test case in a converging duct. For free-stream boundary conditions at the inlet of the duct, the flow quantities at the boundary values are set to the known supersonic free-stream condition. For outflow boundary conditions at the outlet of the duct, since we do not know *a priori* the flow variables after the shock system, we choose physical conditions so that the post-shock region remains supersonic and thus, a Neumann-type extrapolation

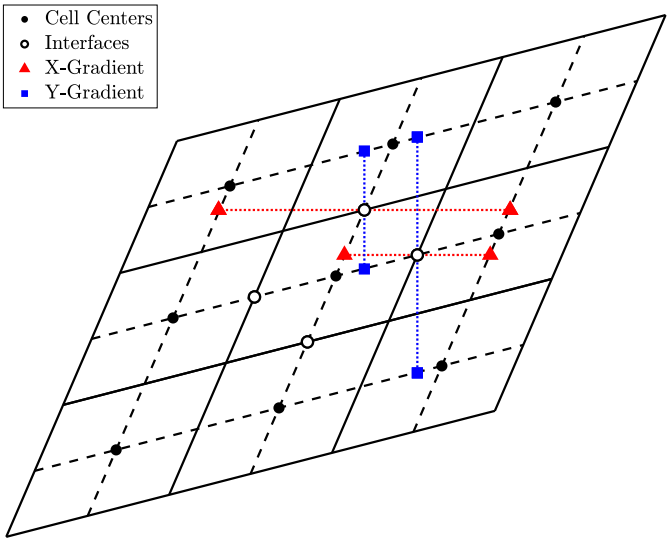

Fig. 1. Schematic describing the calculation of gradient quantities at structured grid interfaces (open circles). Values are linearly interpolated from the cell centers (closed circles) to the auxiliary points at the red triangles and blue squares for calculation of the interface x and y gradients. (For interpretation of the colors in the figure(s), the reader is referred to the web version of this article.)

boundary condition can be used for the outflow. 5-moment systems with subsonic ($M < 1$) flow near the boundaries will necessarily have some information advecting from outside the domain, which is often handled by assigning a flow state outside the domain. Supersonic flows, however, advect all of their information out of the domain. This is generalized to other hyperbolic systems, where the equivalent *supersonic* condition for a boundary on the right is that the lowest wave speed is positive, i.e., moving out of the domain, and similarly for boundaries at other orientations. In the 5-moment system, for a flow that is moving to the right ($+x$ direction), the supersonic condition requires that $u - \sqrt{\gamma p/\rho} > 0$, which clearly leads to $u > \sqrt{\gamma p/\rho}$. However, in the 10-moment system, the leftward-most moving wavespeed is $u - \sqrt{3p_{xx}/\rho}$, which imposes a typically more strict condition: $u > \sqrt{3p_{xx}/\rho}$. Under the assumption that $p_{xx} \approx p$ and $\gamma = 5/3$ (assuming a monatomic gas), the condition that no external information propagates back into the domain in the 10-moment system corresponds to

$$M > \frac{\sqrt{3p/\rho}}{\sqrt{\gamma p/\rho}} = \frac{3}{\sqrt{5}} \approx 1.34. \tag{67}$$

In a duct, there are also walls off of which the fluid must be properly reflected. Previous work [8,13,22] has considered the existence of Knudsen boundary layers which can capture arbitrary slip velocities and temperatures at the wall by incorporation of accommodation coefficients. However, for the purposes of benchmarking the 10-moment model with other fluid models, we assume purely specular reflection at wall boundaries. This slip boundary condition allows for comparison to the results of the Euler equations, for which the exact solution is known. To perform the reflection of the particle velocities off the wall, we approximate the local VDF of the impinging particles from the 10-moment equation system as a Gaussian distribution as shown in Eqn. (21). Observing the form of the equation in two velocity dimensions, we consider the following VDF from the local fluid properties:

$$f^{2D} \simeq \frac{\rho}{m}\left[\frac{\rho^2}{(2\pi)^2\left(p_{xx}p_{yy} - p_{xy}^2\right)}\right]^{1/2} \exp\left[-\frac{\rho}{p_{xx}p_{yy} - p_{xy}^2}\left(p_{yy}w_x^2 - 2p_{xy}w_x w_y + p_{xx}w_y^2\right)\right]. \tag{68}$$

The argument takes the form of a generalized ellipse in $\{w_x, w_y\}$. Thus, contours of constant f are ellipses in velocity space. A specular reflection of this ellipse about the wall corresponds to the reflection of the distribution function after collision with the wall. Namely, if we know the rotation angle of the major axis of this ellipse from the v_x axis, θ, then the post-reflection angle will be $\theta_{post} = \phi + (\phi - \theta_{pre})$, where ϕ is the angle of the wall with respect to the x axis, which corresponds to the relative angle between the wall-oriented velocities $(v_{||}, v_{\perp})$ and the coordinate-axes (v_x, v_y). A schematic of the construction of the post-collisional distribution is shown in Fig. 2. Full equations for θ and post-collision properties are presented in Appendix B. For instance, consider a flow with $T_{xx} > T_{yy} > T_{xy} = 0$, i.e., the distribution is hottest in the x-velocity direction, and $\theta = 0$. If the flow specularly reflects upon a 45° wall (i.e., $\phi = 45°$), the high x-velocity particles become high y-velocity particles after being reflected, and thus the post-collisional distribution becomes hottest in the y-velocity direction and $\theta' = 90°$. In our simulations, we assume $v_z = 0$ and a two-dimensional flow; it is however to be noted that the boundary condition can be generalized to a three-dimensional flow.

Cells that are adjacent to the boundary use the VDF shown in Eqn. (68) to calculate the flux leaving the cell to the wall, and the specularly reflected VDF using post-collision quantities, as illustrated in Fig. 2, to calculate the reflected flux back into the cell due to collisions with the wall. This boundary condition conserves mass, momentum parallel to the wall, and energy.

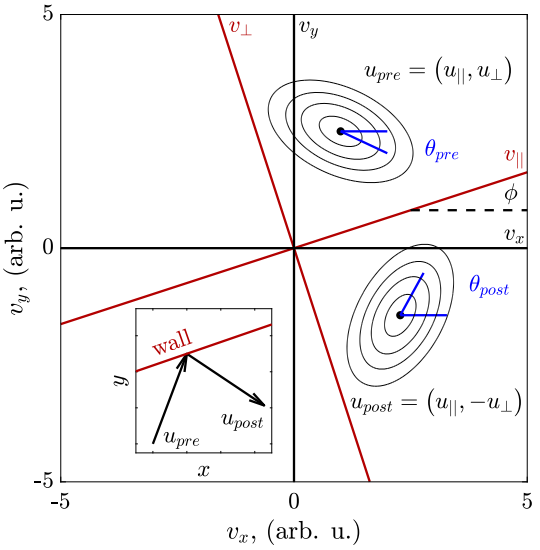

Fig. 2. Illustration of specular reflection boundary condition in 2-D with wall angle ϕ and distribution angle θ.

Table 1
Normal shock initial conditions.

Π	Π_L	Π_R
ρ	1	$4M_L^2/\left(M_L^2+3\right)$
u_x	$M_L\sqrt{5/3}$	$\left(M_L^2+3\right)/\left(4M_L\right)\sqrt{5/3}$
u_y, u_z	0	0
p_{ij}	δ_{ij}	$\delta_{ij}\left(5M_L^2-1\right)/4$

In the 2-D DSMC simulations, the specular condition is similarly employed at all walls to benchmark the DSMC and 10-moment solutions. To ensure a uniform free-stream, particles between a few λ_{MFP} of the inlet are thermalized through artificial collisions according to the free-stream distribution functions [51]. At the outlet, although the flow is supersonic, it was observed from the DSMC results that the presence of negative velocity particles at the tail of the VDFs could affect the results if, like in the fluid simulation, we do not account for any influx of information from outside the domain. For this reason, in the 2-D DSMC runs, the domain size is extended a few λ_{MFP} beyond the outflow boundary of the duct.

4. Case I: one-dimensional steady normal shock

To demonstrate its efficacy, the 10-moment system is compared to the 5-moment Navier-Stokes model and DSMC results under standard compressible fluid dynamics problems.

4.1. Numerical setup

First, we present a standing normal shock with incident Mach number M_L; and initial discontinuity at $x = 0$ with $\mathbf{\Pi} = \{x < 0 : \mathbf{\Pi}_L, x > 0 : \mathbf{\Pi}_R\}$, with left and right states as shown in Table 1. The properties on the right-hand side of the domain have been calculated using the Rankine-Hugoniot equations for post-shock conditions with specific heat ratio $\gamma = 5/3$ to ensure a standing normal shock. The domain is simulated from $x = [-50\lambda_0, +50\lambda_0]$, where λ_0 is the pre-shock mean free path, $\lambda_0 = \tau_L\sqrt{\pi p_L/2\rho_L}$. The number of cells is $N_x = 2000$ for the fluid models and $N_x = 500$ in DSMC. In addition, $T_r = 0.005 \simeq p_L/\left(k_B\rho_L/m\right)$ (cf. Eqn. (48)) and 2.5×10^4 macroparticles per cell are used in DSMC. In plotting, each flow quantity ξ is normalized as

$$\xi' = \frac{\xi - \xi_0}{\xi_1 - \xi_0}, \tag{69}$$

where ξ_0 and ξ_1 are the pre- and post-shock values, respectively, except for the bulk velocity u in which ξ_0 and ξ_1 are chosen to be the post- and pre-shock bulk velocities, respectively, as the flow decelerates across the shock. The x axis is normalized by λ_0, i.e., $x' = x/\lambda_0$.

If $M_L = 1$, then $M_R = 1$ and there is no shock. In this case, one expects a Maxwellian VDF everywhere in the domain. When $M_L > 1$, then $M_R < 1$, causing a shock to appear. If $M_L = 1 + \epsilon$, where $\epsilon \ll 1$, the VDF inside the shock can be approximated as a weak non-Maxwellian. As the 5-moment Navier-Stokes equations are derived assuming $\text{Kn} \ll 1$, it can be expected that 5-moment as well as 10-moment models can capture the shock accurately for $M_L = 1 + \epsilon$. As M_L increases, the shock width increases and more

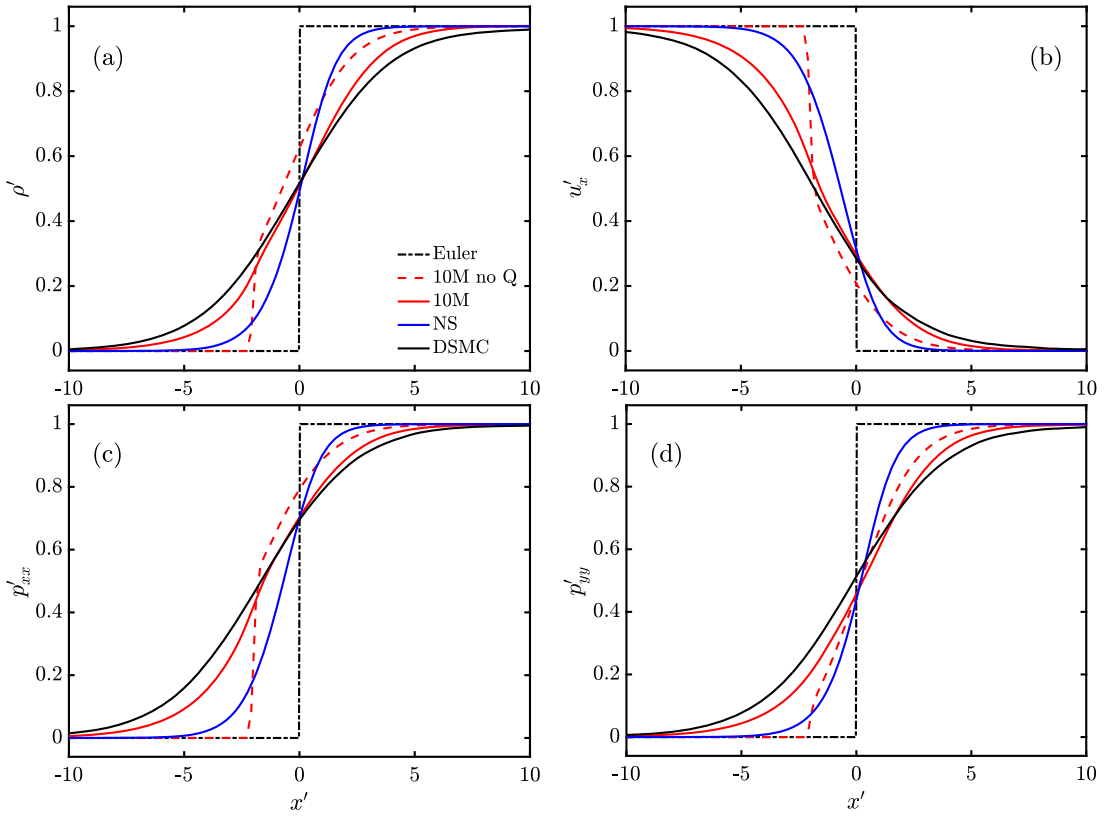

Fig. 3. Normal Mach 2 shock profiles of (a) density, (b) x-velocity, (c) longitudinal pressure (p_{xx}), and (d) transverse pressure (p_{yy}) for the Euler equations, 10-moment without heat flux (10M no Q), 10-moment with heat flux (10M), Navier Stokes (NS), and DSMC.

inter-molecular collisions are required to equilibrate the pre-shock VDFs to the post-shock state. Thus, the VDFs inside the shock becomes more non-Maxwellian. The key hypothesis of this study is that the 10-moment system captures the non-Maxwellian nature within the shock better than the 5-moment Navier-Stokes system and approaches the DSMC (kinetic) results as the Knudsen number increases. However, as M_L further increases, e.g., $M_L > 3$, the VDFs become increasingly non-Maxwellian, beyond which a higher-order moment model is required. The present test case can serve as a benchmarking problem for future investigations of higher-order moment models (e.g., 14-moment). Here, we discuss the results of the standing shock for $M_L = 2$ to illustrate the difference between Navier-Stokes, 10-moment, and DSMC results. Then, we compare the Maxwellian closure with the Gaussian closure. Finally, the differences between Navier-Stokes, 10-moment, and DSMC will be shown for a range of M_L from 1.2 to 4.

4.2. Mach 2 results

4.2.1. Comparison between Navier-Stokes, 10-moment, and DSMC

Fig. 3 shows the (a) normalized density, (b) velocity, and (c, d) on-diagonal pressure tensor components, i.e., p_{xx} and $p_{yy} = p_{zz}$, for the case where the incoming Mach number $M_L = 2$. Results of Euler, Navier-Stokes, 10-moment, and DSMC simulations are shown. The Euler solution exhibits a perfect discontinuity as predicted by the Rankine-Hugoniot relations. In other words, the Euler system describes the limit of fully collisional flow (i.e., $\tau \to 0$) in which there is no finite equilibration region. It is to be noted that two results from the 10-moment system are shown: without and with the heat flux closure as shown in Eqn. (33). Without the heat flux closure (10M no Q), there exists a so-called *frozen* discontinuity at about $x' = -2$, which is consistent with previous literature [58,59]. The discontinuity is analogous to the shocks that occur in the 5-moment Euler system whenever the flow is supersonic, except it now occurs because the upwind Mach number is above the fastest upwind wave speed, i.e., $M > 1.34$ (cf. Eqn. (67)), hence the inviscid portion of the 10-moment system treats this point as a shock. For $M < 1.34$, no frozen discontinuity is seen. Because the heat flux closure, which is parabolic in nature, essentially has an infinite wavespeed, the discontinuity is removed significantly since the heat flux can still transport downstream information upwind.

While being able to capture the finite thickness of the shock, the Navier-Stokes results underpredict the shock width compared to the DSMC results. Here, the results shown are for $M_L = 2$. The finite thickness of the shock is due to the transition from the pre-shock state to the post-shock state causing a non-Maxwellian VDF within the shock. It is interesting to see that the results obtained from the 10-moment with heat flux closure (10M) are in better agreement with the DSMC solution than the 5-moment Navier-Stokes solution. However, it can be seen in Fig. 3 that the width of the shock obtained from the 10-moment solver is slightly underpredicted compared

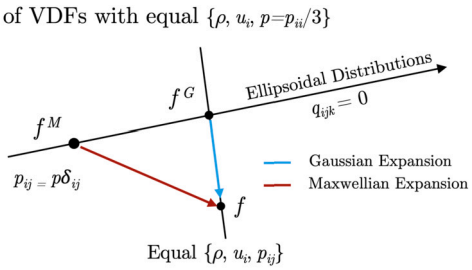

Fig. 4. Function space representation of the approximate distribution functions used to form the system of equations. The true distribution function f can be expanded directly about the equilibrium Maxwellian VDF, f^M, or about the local Gaussian VDF, f^G. Furthermore, the collisional relaxation can be to f^M or f^{ES} for the BGK or ES-BGK operators, respectively.

to the DSMC solution. The discrepancy is most likely due to the heat flux not being a perfect reconstruction, and particularly, an *underprediction* of the kinetic third moment, due to the non-Maxwellian distribution function inside the shock, leading to a thinner shock width. The heat flux will be discussed in more detail in the following section.

At steady state, the conserved quantity ρu is constant through the shock. It can be seen from Figs. 3(a) and (b) that the density and velocity profiles obtained from the 10-moment with heat flux are in better agreement with the DSMC results compared to the 5-moment (NS) results. Interestingly, it is shown that the longitudinal pressure p_{xx} (Fig. 3(c)) is not equal to the transverse pressures $p_{yy} = p_{zz}$ (Fig. 3(d)) inside the shock. As the high-velocity flow first decelerates through collisions with the higher density right state, the gas is heated up in the x direction and then the energy is transferred to the transverse directions by collisions after a finite distance. Hence, it can be seen that $p_{xx} > p_{yy}$ inside the shock from the DSMC and 10-moment results. In both DSMC and 10-moment results, the transverse pressure lags the longitudinal pressure by about $2\lambda_0$. While the results obtained from the 10-moment without heat flux (10M no Q) show a larger numerical shock for p_{xx} than p_{yy}, the heat flux closure assuming a Maxwellian distribution for the equilibrium VDF (10M) removes the numerical discontinuity. While the Navier-Stokes solution underpredicts the shock width compared to the DSMC results, it is interesting to note that the Navier-Stokes solution also captures a degree of pressure anisotropy as $p_{xx} = p - \tau_{xx} = p - \frac{4}{3}\mu\frac{\partial u_x}{\partial x}$ and $p_{yy} = p - \tau_{yy} = p + \frac{2}{3}\mu\frac{\partial u_x}{\partial x}$ for the 1-D simulations, i.e., $p_{xx} > p_{yy}$ due to $\frac{\partial u_x}{\partial x} < 0$ as shown in Fig. 3(b).

4.2.2. Evaluation of heat flux (third-order moment) closure using DSMC (kinetic) results

As can be seen by comparing the results in Fig. 3 for the 10-moment results with and without heat flux, the form of the closure is instrumental to the accuracy of the 10-moment model. For the moment closure (e.g., Chapman-Enskog expansion), an approximation needs to be made for the arbitrary, non-Maxwellian VDF, f, for the right hand side of kinetic transport equation, i.e., the collisional term. In the 5-moment system (e.g., Navier-Stokes equations), it is natural to take the equilibrium function to be a Maxwellian VDF due to the following two reasons. First, the H-theorem states that the VDF becomes a Maxwellian distribution in the presence of fully collisional flow. In other words, the Maxwellian VDF corresponds to the maximum entropy condition in the presence of binary elastic collisions. Second, the 5-moment system solves for ρ, u_i, and p (isotropic pressure) with the inherent assumption that $p_{xx} = p_{yy} = p_{zz} = p$ and $p_{ij} (i \neq j) \ll p$. In addition to the description of f, when considering a BGK type operator, one can also choose the VDF to which f relaxes to through the collisions. While the natural choice is to consider that any f will relax to a Maxwellian VDF f^M due to the H-theorem, the key assumption of the ES-BGK operator is that a non-Maxwellian VDF, f, does not locally relax to f^M. For the reasons described above, in this manuscript, we employ the ES-BGK operator, which provides $\mathrm{Pr} = 2/3$ when choosing $\eta = -1/2$ in Eqn. (22), so that a better benchmarking can be performed between the fluid and kinetic results.

In contrast, previous investigations for 10-moment and 14-moment systems [47,60,61] proposed and employed a *Gaussian* heat flux closure. Reference [47] also developed an 'entropy-respecting' closure by beginning from the requirement that the closure increase entropy, and making simplifying assumptions to obtain a closed form with one free parameter. However, since no results using the closure were presented, we do not make comparisons to the model in this paper.

The Gaussian heat flux closure is based on the assumption that the equilibrium distribution about which the perturbative expansion should be made is an anisotropic Gaussian distribution:

$$f = f^G(1 + \xi\phi_{1,g} + \ldots), \tag{70}$$

where f^G is a Gaussian distribution, equivalent to the ellipsoidal distribution when $\wp = p_{ij}$ as shown in Eqn. (21). In the framework of the 10-moment system, the Gaussian distribution is an extension of the Maxwellian distribution which considers all of the state variables in the 10-moment system, i.e., ρ, u_i, and p_{ij}. The Gaussian distribution is also a natural choice to be used in conjunction with the ES-BGK collision operator, as it assumes that the non-Maxwellian VDF, f, is a perturbation from a Gaussian distribution as shown in Eqn. (70) and relaxes to a different Gaussian distribution [31].

Fig. 4 shows the relation between the Maxwellian and Gaussian distributions. Let us consider a non-Maxwellian VDF, f, while a given set of first five moments $\{\rho, u_i, \text{and } p = p_{ii}/3\}$ is considered. In this function space, it is to be noted that the anisotropic pressure tensor, p_{ij}, the heat flux, q_{ijk}, and the higher order moments (e.g., kurtosis) can be any physically permissible values. If one calculates the anisotropic pressure tensor (p_{ij}) from f, it can be considered that f and f^G lie in the same subspace (represented as the vertical line in Fig. 4) in which the first ten moments, $\{\rho, u_i, p_{ij}\}$, are equal; meanwhile, the Maxwellian VDF f^M has a

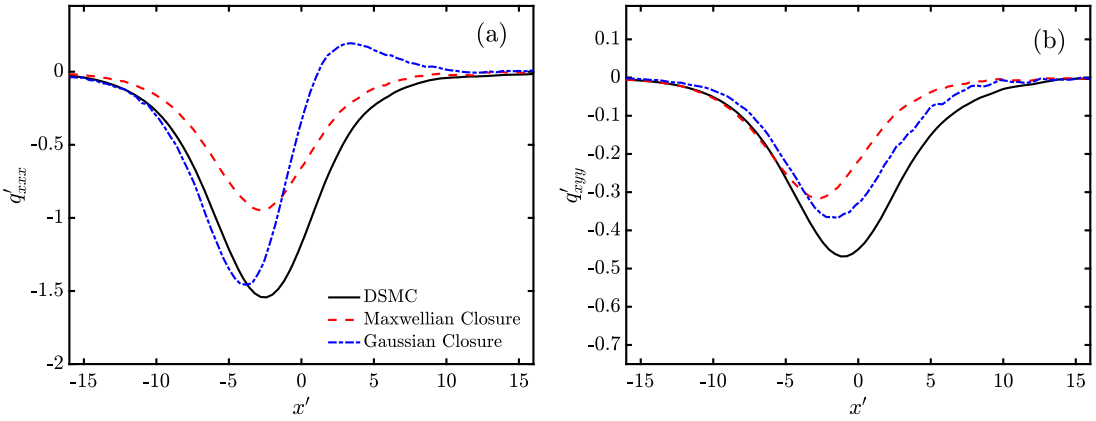

Fig. 5. Assessment of the heat flux $\langle v_i v_j v_k \rangle$ directly obtained from the DSMC results ($M = 2$) in comparison to the heat flux closure models using Maxwellian and Gaussian distributions as the equilibrium VDF in the ES-BGK collision model, (a) q_{xxx} and (b) q_{xyy}.

different pressure tensor from f, i.e., $p_{ij} = p\delta_{ij}$. Through f^G and f^M can be defined the subspace of ellipsoidal distributions as shown in Eqns. (21) and (22), where the line is defined by the free parameter, η. It is known that the Maxwellian VDF corresponds to the maximum entropy condition from the H-theorem that accounts for the Boltzmann collision integral. Thus, from a physical perspective, a non-Maxwellian VDF relaxes towards a Maxwellian VDF through elastic binary collisions. Furthermore, it is shown in Ref. [47] that the Gaussian VDF f^G maximizes entropy given the (not-physically justified) constraint that the full pressure tensor p_{ij} is conserved in addition to ρ and u_i. This corresponds to a larger entropy than the one calculated from f, but a smaller entropy compared to the Maxwellian VDF f^M, which has the looser constraint that only p must be conserved. Note that the ellipsoidal distribution f^{ES} in Eqn. (21) is used solely when considering the BGK operator (which is chosen for mathematical simplicity and is physically inaccurate compared to the Boltzmann collision operator) so that the Prandtl number can be tuned to be physical. While the ES-BGK model is not the same as the Boltzmann collision model, we consider this model to be sufficient for the purpose of demonstrating the 10-moment model and benchmarking with the DSMC results.

The Gaussian perturbative expansion with the ES-BGK operator results in the following equation for the Gaussian heat flux [46]:

$$q^G_{ijk} = -\tau \left[p_{kl} \frac{\partial}{\partial x_l} \left(\frac{p_{ij}}{\rho} \right) + p_{jl} \frac{\partial}{\partial x_l} \left(\frac{p_{ik}}{\rho} \right) + p_{il} \frac{\partial}{\partial x_l} \left(\frac{p_{jk}}{\rho} \right) \right], \tag{71}$$

which is contrasted with the Maxwellian formulation as shown in Eqn. (33).

The third moment term from the kinetic (DSMC) results is compared with the heat flux closure models for 10-moment systems. Fig. 5 shows the comparison of q_{xxx} calculated using the following three approaches:

- Third moment ($q_{ijk} = m \int w_i w_j w_k f d^3\mathbf{v}$) directly from the DSMC results;
- Heat flux assuming isotropic Maxwellian closure, as shown in Eqn. (33), using ρ, u_i, and p obtained from the DSMC results;
- Heat flux assuming anisotropic Gaussian closure, as shown in Eqn. (71), using ρ, u_i, and p_{ij} obtained from the DSMC results.

Additionally, τ in Eqns. (33) and (71) are calculated using Eqn. (49). It can be seen in Fig. 5 that q_{xxx} with Maxwellian closure is underpredicted but maintains the right profile compared to the q_{xxx} directly from the DSMC simulation. The heat flux component q_{xxx} calculated using the Gaussian closure is closer to DSMC particularly in the pre-shock regime but the biggest drawback is the presence of the wrong sign ($q'_{xxx} > 0$), which can be seen downstream of the shock (e.g., $x' \approx 3$) as shown in Fig. 5(a). Similarly, Fig. 5(b) shows that q_{xyy} assuming the Maxwellian closure is smaller than the DSMC results, while that assuming the Gaussian closure is closer to the DSMC results. However, the most notable difference is that the Maxwellian closure provides a good agreement with DSMC results in the pre-shock region, e.g., $x' < -5$, as shown in Fig. 5(b).

The discrepancy of the heat flux closures can be explained by differences in the temperature gradient. The Gaussian closure for q_{xxx} can be written in 1-D as,

$$q^G_{xxx} = -3\tau p_{xx} \frac{\partial}{\partial x} \left(\frac{p_{xx}}{\rho} \right), \tag{72}$$

and the Maxwellian closure yields

$$q^M_{xxx} = -3\tau p \frac{\partial}{\partial x} \left(\frac{p}{\rho} \right). \tag{73}$$

A negative q^M_{xxx} as shown in Fig. 5(a) illustrates that the isotropic temperature ($T = p/nk_B$) is monotonically increasing across the shock. On the other hand, the sign of q^G_{xxx} flips due to the fact that the longitudinal temperature ($T_{xx} = p_{xx}/nk_B$) has a maximum peak (overshoot) inside the shock. In the Maxwellian closure, the heat flux represents the perturbation from an isotropic Maxwellian

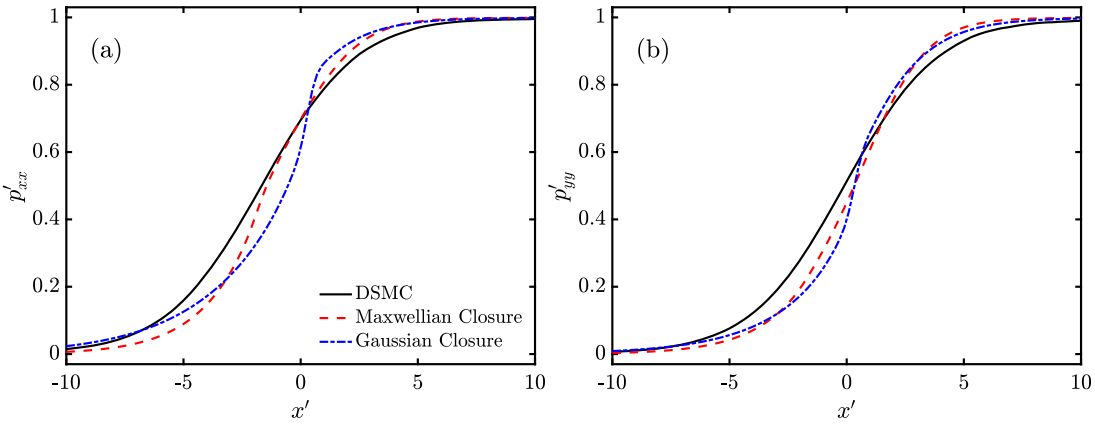

Fig. 6. Comparison of DSMC to 10-moment fluid results using Maxwellian and Gaussian for Chapman-Enskog expansion showing (a) p'_{xx} and (b) p'_{yy} in a Mach 2 normal shock.

distribution, and the heat flux can be interpreted as the transfer of total energy throughout space. In the Gaussian closure, the heat flux components decouple each velocity dimension so that, for instance, q_{xxx} is a function of only derivatives of p_{xx} and not p_{yy} or p_{zz}. During the spatial transport (i.e., from one cell to the next), the distribution is undergoing collisional relaxation, and the full pressure tensor is not conserved. Therefore, in the presence of anisotropy, it is not physical to use gradients in p_{xx} alone, since it cannot be said to be purely advected in the presence of collisions and thus a holistic description, coupling all three pressure components is more physically accurate for gasdynamic flows with binary elastic collisions. The present study shows that the recommended procedure to evaluate the high-order moment terms is to compare with those obtained from a kinetic model.

4.2.3. Effects of heat flux closure on 10-moment simulations

Fig. 6 shows a comparison of the anisotropic pressure profiles (p_{xx} and p_{yy}) obtained from 10-moment simulations of the Mach 2 normal shock using the Maxwellian and Gaussian closures. Note that the DSMC results shown in Fig. 6 are identical to those in Figs. 3(c) and (d). Overall, the 10-moment system with a Maxwellian closure (red dashed lines) captures the shock structure, while there are visible discrepancies with DSMC results in the upstream of shock (i.e., $x' < 0$).

The 10-moment model assuming a Gaussian closure (blue lines) shows a shock profile being broadened upstream and thinned downstream, particularly for p_{xx}, as shown in Fig. 6(a). This reflects the fact that the heat flux assuming a Gaussian closure, q^G_{xxx}, is overestimated in the upstream and underestimated in the downstream. Near the center of the shock (i.e., $x' \approx 1$), where the Gaussian estimate of q_{xxx} changes sharply and crosses zero, there is a steep change in the curvature of p_{xx}. The fact that the Gaussian closure results in a reversal of the sign of q_{xxx} in the downstream of the shock creates a much larger discrepancy with the DSMC solution than the Maxwellian closure; over the 10%-90% width of the DSMC shock, the L_2 discrepancy in the profile of p_{xx} using the Gaussian closure is 2.4 times that of the profile using the Maxwellian closure. As shown in Fig. 6(b), the Maxwellian and Gaussian closures for q_{xyy} exhibit similar trend as q_{xxx}, i.e., q_{xyy} is slightly more steepened with the Gaussian closure than with the Maxwellian closure. The discrepancy in p_{xx} has cascading effects up the chain of moments, leading each of the primitive variables to have the same strong change in curvature. For completeness, comparisons of the profiles of ρ and u_x are presented in Appendix C. While the differences in the estimates of q_{ijk} may be subtle in this test case, an estimate of the heat flux is often a key model output in wall-bounded supersonic or reacting flows and has a strong effect on all of the flow variables. Thus, it is important to be able to capture the order of magnitude and especially the direction of heat flow.

4.3. Parametric study of various Mach numbers

Fig. 7 shows the results of the normal steady shock case for five different incoming Mach numbers, $M_L = 1.2$, 1.4, 2.4, 3.0, and 4.0. As expected, the 5-moment Navier-Stokes, 10-moment, and DSMC results are in agreement at small M_L cases, e.g., $M_L = 1.2$ and 1.4, as shown in Figs. 7(a) and (b), respectively. This is because the deviation of the non-Maxwellian VDF from a Maxwellian VDF is not significant within the shock for M_L close to 1. Thus, a linear perturbation of the Maxwellian VDF, i.e., the Navier-Stokes model, sufficiently captures the non-Maxwellian nature. It is to be noted that the Navier-Stokes model is in slightly better agreement with DSMC than the 10-moment results in Fig. 7(a). This is due to the fact that the Navier-Stokes model is using the higher-fidelity Boltzmann closure, which is more accurate in the near-equilibrium regime where the small-Kn assumption is valid. It is expected that a 10-moment model with closure using the Boltzmann collision integral would converge to the Navier-Stokes and DSMC results; this is reserved for future investigation. As the Mach number increases, the decrease in the shock width can be seen using all three models. Because the shock width (L_s) is the key characteristic length in the problem, the associated Knudsen number ($\mathrm{Kn}_s = \lambda / L_s$) increases with Mach number. Accordingly, it can be seen that the Navier-Stokes model, which assumes $\mathrm{Kn} \ll 1$, is in poorer agreement with DSMC results than the 10-moment model, especially as the incoming Mach number and Kn_s increase, as shown in Figs. 7(c)–(e). At $M_L = 1.4$, the Navier-Stokes results begin to deviate from the DSMC results, while the 10-moment is in good agreement with

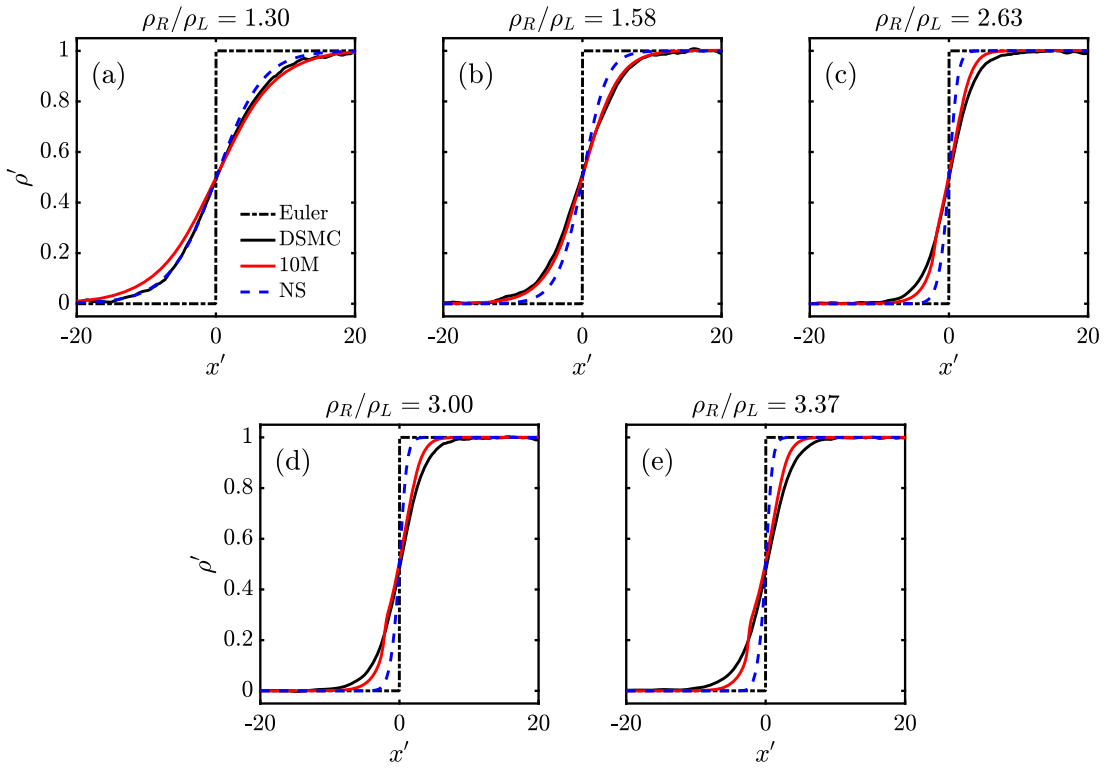

Fig. 7. Density profiles for incoming Mach number M_L = (a) 1.2, (b) 1.4, (c) 2.4, (d) 3.0, and (e) 4.0 using fluid (Euler, Navier-Stokes, and 10-moment with Maxwellian heat flux closure) and DSMC simulations. The density jump across the shock (ρ_R/ρ_L) is also shown for each case.

the DSMC results, as shown in Fig. 7(b). This demonstrates how the 10-moment model, as formulated, is better able to capture the non-Maxwellian effects than the Navier-Stokes equations with approximate closure for anisotropic pressure elements. As seen in the previous section, by $M_L = 2$ (see Fig. 3), the 10-moment results begin to deviate from the DSMC results. Fig. 7(c) corresponds to $M_L = 2.4$, which shows a smooth transition from $M_L = 2$, as shown in Fig. 3. At $M_L = 3$, a larger difference between the 10-moment and DSMC results can be seen throughout the shock (see Fig. 7(d)). In addition, around $x' \approx -2.5$, a numerical discontinuity can be seen from the 10-moment results. Recall from Fig. 3 that there exists a frozen discontinuity when using the 10-moment model without the heat flux due to flow travelling faster than $M = 1.34$, as described in Section 4.2. Upstream of that point, $\mathbf{F}^- = 0$ in Eqn. (63), so downstream flow $\left(\mathbf{U}^R\right)$ can only influence the fast-moving flow through the heat flux closure. It can be considered that the 10-moment closure underestimates the heat flux (i.e., the third moment) in an increasingly nonequilibrium flow and cannot sufficiently transfer information upstream. As the Mach number further increases, e.g., to $M_L = 4$ as shown in Fig. 7(e), the deviation between the fluid (10-moment and 5-moment Navier-Stokes) and kinetic (DSMC) results increases. However, the 10-moment results with the Maxwellian heat flux closure continue to perform better than the Navier-Stokes results in comparison to the DSMC results. It is to be noted that the 10-moment simulation can be run at higher Mach numbers, but the numerical discontinuity becomes more evident. This suggests that at higher Mach numbers the flow becomes increasingly non-Maxwellian and one may need to take higher-order moments (e.g., 14-moments), use a higher-order perturbation to the distribution function (cf. Eqn. (26)), or develop a specialized closure to capture the non-Maxwellian VDFs in high-Mach number shocks.

5. Case II: one-dimensional unsteady shock tubes

5.1. Sod shock tube

The normal shock results presented in Section 4 achieved steady-state, for which the normalized results are independent of the choice of relaxation time τ_0 since the shock width is proportional to λ_0 and thus τ_0. The Sod Shock tube, whose solution in the Euler system consists of a self-similar *unsteady* solution, is a well-accepted test case for the development of Euler solvers [62]. Because the problem is time-dependent, the choice of the relaxation time τ_0 will affect the results at a particular time, i.e., the smaller τ_0, the more collisional the flow is, and the larger τ_0, the less collisional the flow is, making the flow more rarefied. For the Sod Shock tube problem, the initial conditions to the left and right of the discontinuity are shown in Table 2.

The domain is simulated from $x = [-1, 1]$; the number of cells is $N_x = 2000$ for the fluid models and $N_x = 500$ in DSMC. Again, $T_r = 0.005$ and 2.5×10^4 macroparticles per cell are used in DSMC. The Navier-Stokes results at varying Mach number have been

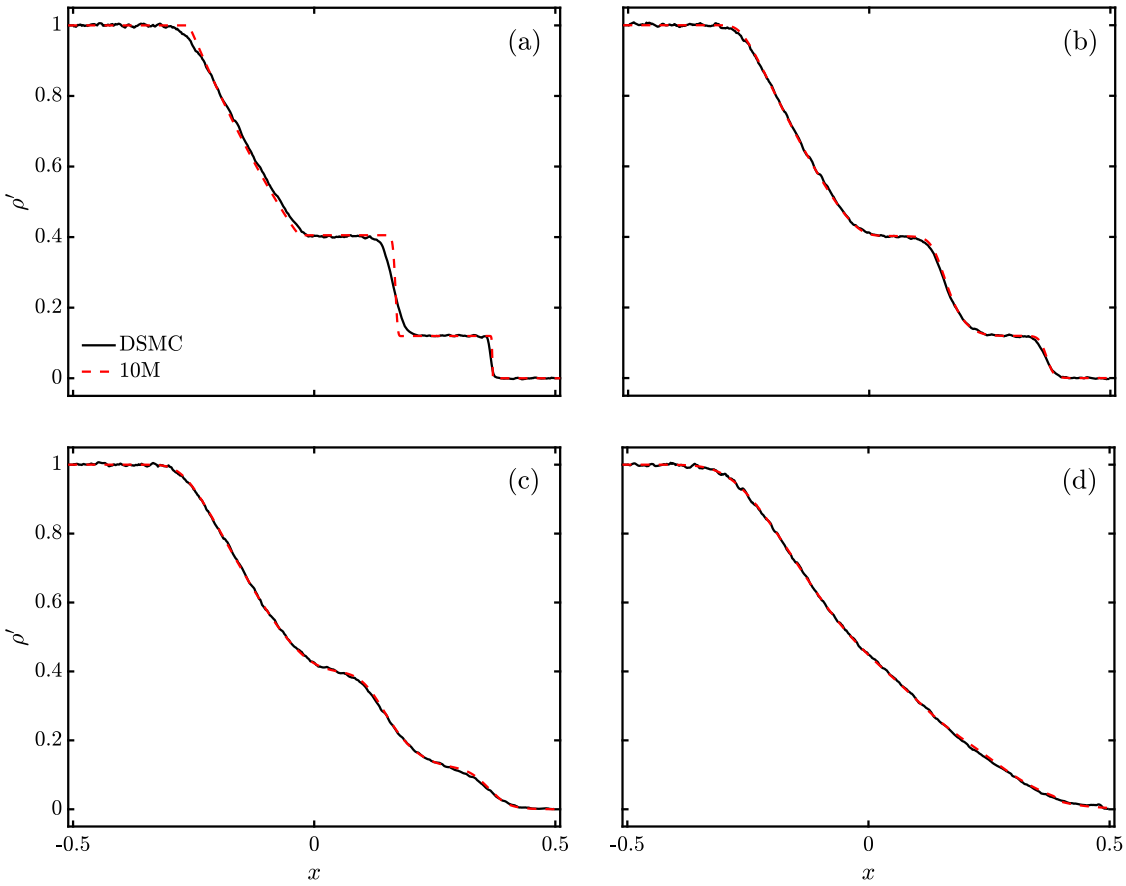

Fig. 8. Normalized Sod shock tube: density profiles for time $t = 0.2$ for τ_0 = (a) 2×10^{-5}, (b) 2×10^{-3}, (c) 5×10^{-3}, and (d) 2×10^{-2}.

Table 2
Sod shock tube initial conditions.

Π	Π_L	Π_R
ρ	1	0.125
u_x, u_y, u_z	0	0
p_{ij}	δ_{ij}	0.1 δ_{ij}

previously benchmarked against high-fidelity Boltzmann equation solvers [63,64]. Instead we focus on a comparison between the 10-moment and DSMC results.

Fig. 8 shows the results of multiple simulations to $t = 0.2$ with varying τ_0. As $\tau_0 \to 0$, the fluid equilibrates quickly and one approaches the Eulerian limit (i.e., $t/\tau_0 \to \infty$), exhibiting sharp discontinuities between the regions, as shown in Fig. 8(a). We note that around the boundaries of each region in the flow, particularly the contact discontinuity (CD), the DSMC solution shows some finite widening not captured by the fluid models caused by kinetic diffusion of particles between the two regions. As found in Ref. [65], the normalized width of a contact discontinuity $\Delta' = (\text{CD width})/\lambda \propto t/\tau$ as more high-velocity particles cross the discontinuity and equilibrate. However, because $\lambda \propto \tau$, the width of the contact discontinuity after the same amount of time, e.g., $t = 0.2$, is roughly unchanged over a wide range of collisionality. Additionally, the DSMC results show a similar kinetic mixing near the edges of the rarefaction wave and shock. These kinetic effects are not captured by the 10-moment model for collisional flows (as τ_0 decreases).

As τ_0 increases, the 10-moment fluid model does not fully reach local equilibrium by the given time, $t = 0.2$. In other words, t/τ_0 decreases, and equivalently, the Knudsen number increases ($\text{Kn} \approx \tau_0/t$), indicating that the average number of collisions that particles undergo during the flow advection decreases. Instead of forming sharp discontinuities, Fig. 8(b) exhibits some widening of the shock and contact discontinuities due to mixing of the distributions on either side of each discontinuity. However, the 10-moment results are in good agreement with the DSMC results for all wave features, i.e., rarefaction, contact discontinuity, and shock. In Fig. 8(c), there is no distinguishable uniform region between the locations of the inviscid discontinuities and thus cannot be considered to be separate discontinuities in this regime. As demonstrated in Fig. 8(d), in the collisionless limit (i.e., $t/\tau_0 = 10$), the discontinuous wave features are not present at all, and the system is dominated by collisionless mixing. If we define the characteristic length scale

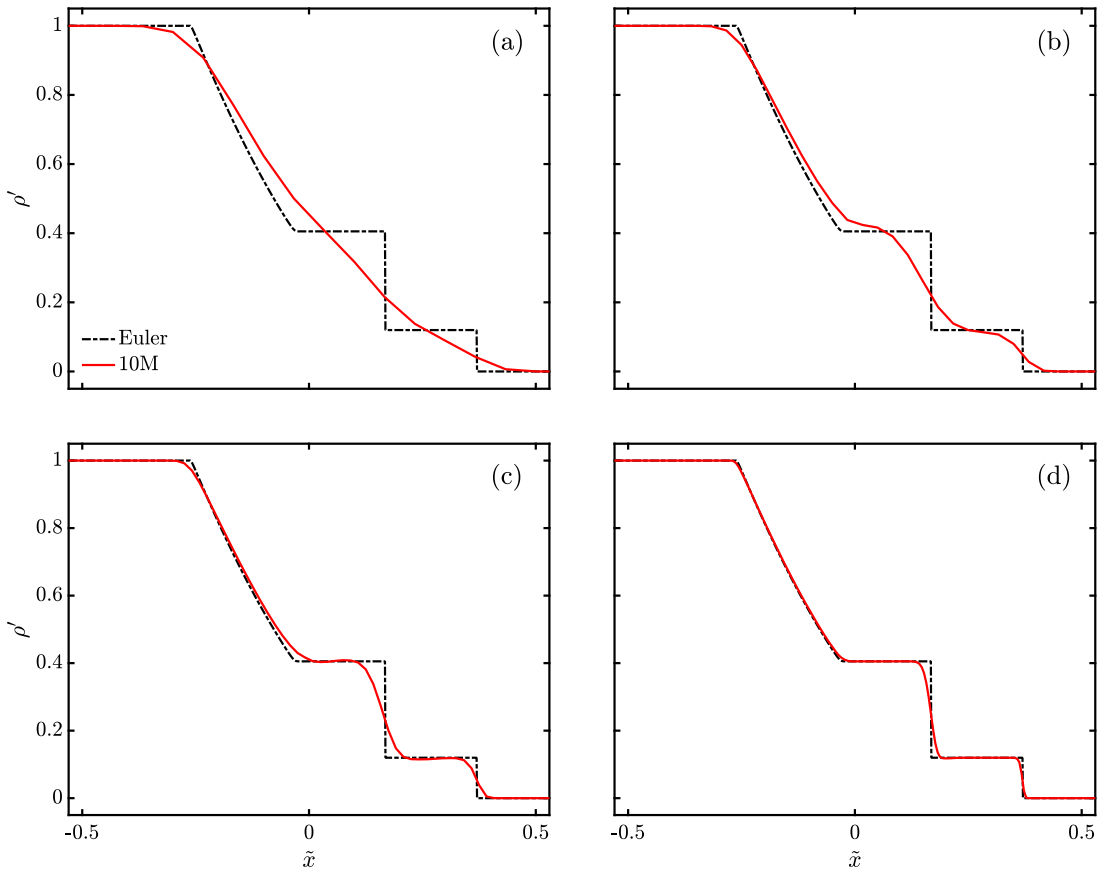

Fig. 9. Normalized 10-moment Sod Shock density profiles for $\tau_0 = 2 \times 10^{-5}$ (red solid) compared to Euler solution (black dashed) at times (a) $t = 3 \times 10^{-3}$, (b) $t = 6 \times 10^{-3}$, (c) $t = 12 \times 10^{-3}$, and (d) $t = 40 \times 10^{-3}$.

by $L = t\sqrt{8p/\pi\rho}$, which corresponds to the distance the average particle will travel in a given time, then the Knudsen number in this flow is approximately $\mathrm{Kn} = \pi\tau/4t \approx 0.08$, well in the regime of the transition from continuum to free-molecular flow. We note that the 10-moment model has qualitatively good agreement with DSMC to this relatively high value for the Knudsen number, i.e., $\mathcal{O}(10^{-1})$. Fig. 9 shows the evolution of the density distribution for $\tau_0 = 2 \times 10^{-5}$, which is identical to Fig. 8(a). Here, the results are shown at different times, $t = 0.003$, 0.006, 0.012, and 0.04. For smaller values of t/τ_0, one expects a rarefied solution (large Kn). As t/τ_0 increases, the flow becomes more collisional as it advects (small Kn). Recall that in the Eulerian solution, the discontinuities are formed in the first instant and the solution is self-similar in time, i.e., any flow quantity $Q(x,t) = Q(x/t)$. Thus, if we rescale x axis of the Euler solution with

$$\frac{\tilde{x}(t)}{t} = \frac{x}{t_0}, \tag{74}$$

then the scaled solution of the Euler equation, $Q(\tilde{x},t)$, is independent of time. Fig. 9 scaled with $t_0 = 0.2$ shows the dynamic relaxation of 10-moment solutions from the initial discontinuity. After a short time, Fig. 9(a), i.e., $t/\tau_0 = 150$, the fluid does not have enough time to equilibrate, resulting in a smooth transition between the pre- and post-shock states. This resembles a more rarefied solution (cf. Fig. 8(d)). However, the comparison between Figs. 8(d) and 9(a) is not exact because the 10-moment results are not self-similar under any linear scaling, due to the fact that the distribution function relaxes to equilibrium exponentially in time, while the advective transport occurs linearly. Thus, the comparison between Figs. 8 and 9 can only be qualitative. As time progresses, as shown in Figs. 9(b) and (c), i.e., $t/\tau_0 = 300$ and 600, respectively, the uniform regions begin to form as the flow comes to equilibrium and discontinuities gradually develop as collisions play a greater role on longer time scales. Eventually, after a long time, the solution approaches the Euler solution, as shown in Fig. 9(d) ($t/\tau_0 = 2000$). This demonstrates the ability of the 10-moment model with Maxwellian heat flux closure to capture elements of the transition from kinetic to continuum-dominated flows.

5.2. Shear flow

Up to this point, we have only made use of the anisotropy of on-diagonal pressure components (normal stress). To further showcase the capabilities of the 10-moment model, we consider a pure shear test case, where the discontinuity is only in the transverse y velocity. The states across the initial discontinuity are shown in Table 3. The discontinuity only in u_y ensures that there

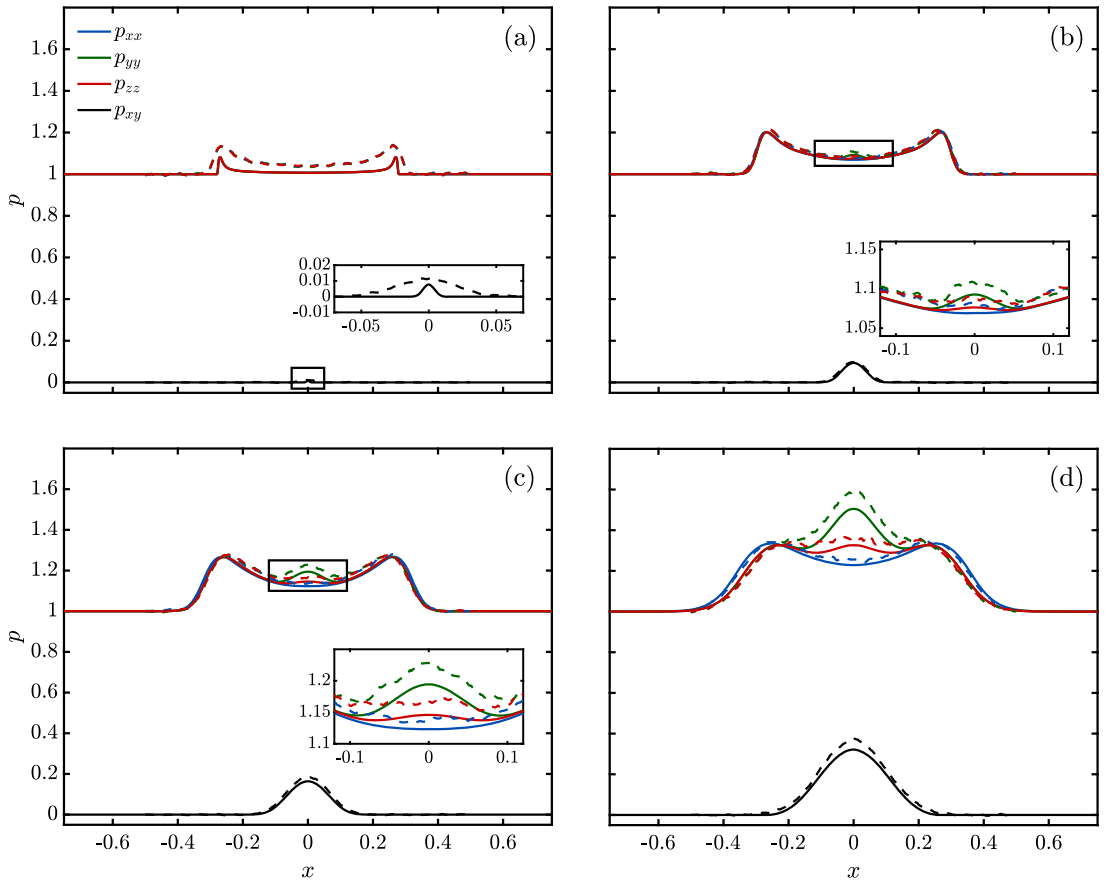

Fig. 10. Results of the pure shear test case at time $t = 0.2$ for τ_0 = (a) 2×10^{-5}, (b) 2×10^{-3}, (c) 5×10^{-3}, and (d) 2×10^{-2}. Solid: 10-moment, dashed: DSMC.

Table 3
Pure shear initial conditions.

Π	Π_L	Π_R
ρ	1	1
u_x, u_z	0	0
u_y	2	−2
p_{ij}	δ_{ij}	δ_{ij}

is no difference in density or temperature difference across the discontinuity, and no advected flow to induce mixing. In the Euler system, such initial shear condition does not result in a formation of waves and there would be no evolution of the flow because u_x and p are identical. If viscosity is taken into account, i.e., the Navier-Stokes system, the deviatoric stresses $t_{xy} = \mu \frac{\partial u_y}{\partial x}$ in Eqn. (56) would lead to a diffusion of u_y, while the 10-moment model captures the shear directly. The simulated domain is from $x = [-1, 1]$ with $N_x = 2000$ for fluid and $N_x = 500$ for DSMC and with $T_r = 0.005$ and 2.5×10^4 macroparticles per cell.

Fig. 10 shows the results of the shear flow simulations for various values of τ_0 at the same t, i.e., $t = 0.2$. All cases exhibit a positive p_{xy} near the centerline, the magnitude of which grows with τ_0. The positivity of p_{xy} can be explained from a fluid perspective by observing Eqn. (10) and noting that from the initial conditions, $\frac{\partial p_{xy}}{\partial t} = -p_{xx} \frac{\partial u_y}{\partial x}$; because $p_{xx} > 0$ and $\frac{\partial u_y}{\partial x} < 0$, p_{xy} grows. For a kinetic explanation of this result, let us consider the expected distribution function at that point. At the centerline, there is mixing between particles from the left region moving right and flow from the right region to the left. Those from the left region have positive y velocities, as well as positive x velocities (corresponding to a positive wave speed); while those from the right region have negative x and y velocities. Thus, there is a correlation of high x and high y velocities and $\langle v_x v_y \rangle > 0$. From a Navier-Stokes perspective, $p_{xy} \simeq -t_{xy} = -\frac{\partial u_y}{\partial x} > 0$. Fig. 10(a) shows the results at low $\tau_0 = 2 \times 10^{-5}$ and, similarly to Fig. 8(a), shows discrepancies between 10-moment and DSMC results. In this regime, the fluid model underpredicts the kinetic effects and reverts to a more wave-like structure. While Fig. 10(a) shows that $p_{xx} = p_{yy} = p_{zz}$ and hence the flow is collisional due to small τ_0, the discrepancy between p_{xx}, p_{yy}, and p_{zz} increases as τ_0 increases, i.e., as flow becomes more rarefied, as shown in Figs. 10(b–d). It can be expected that the Navier-Stokes equations, which consider $p_{ij} \simeq p\delta_{ij}$, cannot accurately capture such large pressure anisotropy. Figs. 10(b–c) show good agreement

Table 4
2-D oblique shock initial and inflow conditions.

	Π_0 at $x = 0$
ρ	1.6103 kg/m^3
u_x	836.5 m/s
u_y, u_z	0
p_{ij}	δ_{ij} 10^5 Pa
T_{ij}	δ_{ij} 300 K
M	2.6

between the 10-moment and DSMC results, indicating that the 10-moment model is able to capture the dynamics of shear-driven flows and the resultant effects on the full pressure tensor. Fig. 10(d) shows results a high value of $\tau_0 = 2 \times 10^{-2}$, where there is still good agreement, but the 10-moment model begins to underpredict the kinetic effects that dominate at low collisionality.

The on-diagonal components of p_{ij} (i.e., $p_{ij|i=j}$) exhibit two distinct features. First, the on-diagonal pressures increase at the centerline as the flow becomes more rarefied. Second, the pressure front moves outward from the centerline, with the wavefront being more diffusive (and hence slightly faster) when the flow is rarefied than when the flow is collisional. To explain the structure of the on-diagonal pressure elements, let us consider the flow dynamics from a kinetic perspective. At the centerline, the presence of counterstreaming particles from either side of the interface corresponds to a large p_{yy} as the VDF in y velocity results in a wide spread due to the counterstreaming velocities (cf. shear). The increase in p_{yy} is then transferred to the other pressure components p_{xx} and p_{zz} through collisions, causing the observed increase in all three pressure components, which can be particularly seen in Figs. 10(b–d) in which τ_0 is large, i.e., flow becomes less collisional. However, the increased pressure at the centerline also induces an outward moving acoustic wave in the x direction. Additionally, the heat flux q_{xxx} is larger than q_{xyy} and q_{xzz}, as shown in Eqn. (33), resulting in a faster diffusion of p_{xx} compared to p_{yy} and p_{zz}. For these reasons, at the centerline, we see that p_{yy} is the highest and p_{xx} is the lowest. Accordingly, p_{zz} is smaller than p_{yy}, but is larger than p_{xx}. Furthermore, as can best be seen in Fig. 10(d) at $x \approx \pm 0.3$, in the outwardly moving pressure wave, like in the normal shock case, $p_{xx} > p_{yy} \approx p_{zz}$ as the flow in the x direction is converted into internal energy.

6. Case III: two-dimensional steady flow: oblique and reflected shocks

The 10-moment and DSMC models are extended to a two-dimensional shock system. The two models are benchmarked under a test case that is a supersonic flow in a channel impinging on a ramp of turning angle 8 degrees. The first test case has an incoming mach number of $M = 2.6$; this supersonic flow generates an oblique shock, which reflects off of the top wall and then exits the domain. The focus of this section is to verify the 10-moment model in the limit of low Knudsen number where the Navier-Stokes results are comparable to DSMC. The second test case increases the Mach number to demonstrate the capabilities of the 10-moment model in two-dimensions in more non-equilibrium regimes.

6.1. Numerical setup

The channel is 1.5 m wide in y direction; begins at $x = 0$ and the 8° ramp starts after 0.5 m and the channel is cut off at $x = 4$ m. For the first test case, the initial Mach number is chosen to be $M_L = 2.6$ to ensure that the flow at the outlet is always faster the fastest wave speed and there can be no information passed back into the domain (cf. Eqn. (67)). The initial and inflow (from the left) conditions, constant throughout the domain, are shown in Table 4.

In the fluid simulations, the number of cells in the x and y directions, $[N_x, N_y] = [400, 150]$, while for DSMC, $[N_x, N_y] = [200, 75]$, with reference temperature 300 K and the number of macroparticles per cell approximately 500. For both fluid and kinetic models, the simulation timestep is 10^{-6} s, which is about $0.1\tau_0$ for high-collisionality case and corresponds to a maximum CFL number of 0.08, satisfying the CFL condition shown in Eqn. (66). Moreover, in the DSMC simulations, to reduce the statistical noise due to finite macroparticles, we take time-averaged results over 5.0 s after steady state, which corresponds to $10^4\tau_0$ in the low collisionality case. To speed up the kinetic simulations, message passing interface (MPI) and domain decomposition in the x direction is used. The wall time for the DSMC simulations is about 48 hours each using 20 processors, while each 10-moment simulation took about 4 hours on a serial processor.

6.2. Comparison between Navier-Stokes, 10-moment, and DSMC results

Fig. 11 shows the results of simulations varying the relaxation time using Navier-Stokes, 10-moment, and DSMC models. The free stream Mach number *normal* to the (first) oblique shock is about $M_{0n} = 1.3$ (in the Euler system), indicating a fairly weak shock. Note that for high collisionality, as shown in Fig. 11(a), the two (the first oblique and the reflected) shocks are sharp discontinuities and match the solutions of the Euler equations. In this case, $L = \mathcal{O}(1\text{ m}) \gg \lambda_0 \approx 3 \times 10^{-3}$ m, and so the width of the shock is small compared to the domain size. At an intermediate collisionality, e.g., Fig. 11(b), $\lambda_0 \approx 3 \times 10^{-2}$ m, so that the shock width $\sim 10\lambda_0$ is visibly broader and within an order of magnitude of the domain; however, the shock width is still smaller than the domain and so the two shocks are still distinguishable from one another, though broadened. Finally, at low collisionality, e.g., Fig. 11(c),

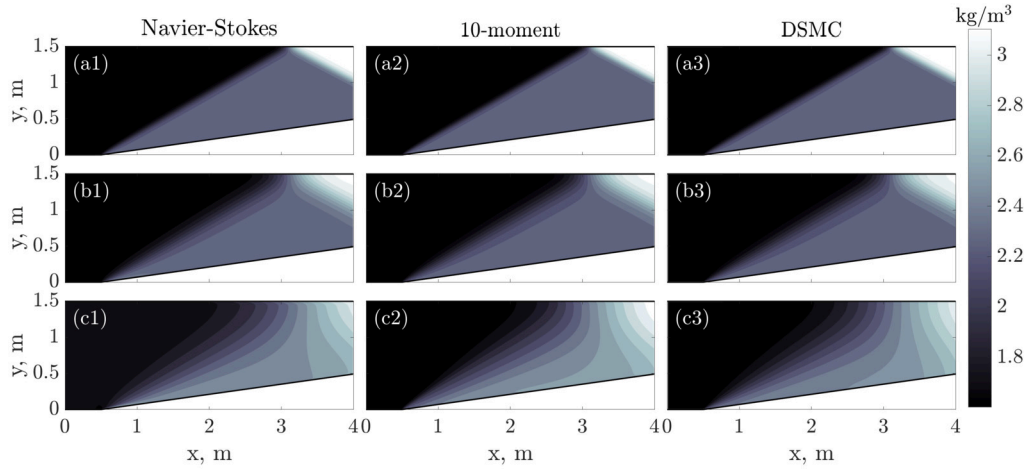

Fig. 11. Mass density profiles of the Mach 2.6 two dimensional ramp with τ_0 = (a) 1×10^{-5} s, (b) 1×10^{-4} s, and (c) 5×10^{-4} s. Showing a comparison between (1) Navier-Stokes, (2) 10-moment, and (3) DSMC simulations.

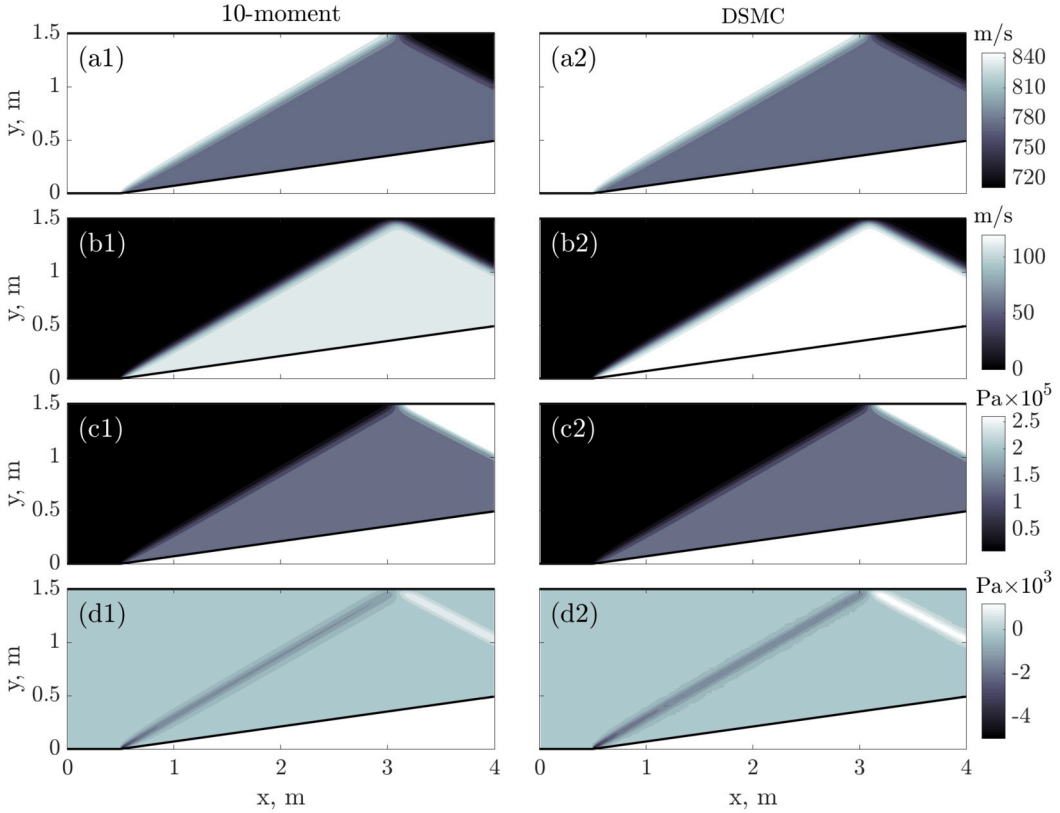

Fig. 12. Full (1) 10-moment and (2) DSMC results for the Mach 2.6 case with $\tau_0 = 1 \times 10^{-5}$ s (high collisionality case), showing (a) u_x, (b) u_y, (c) p_{xx}, and (d) p_{xy}. See Fig. 11(a2) and (a3) for the profiles of ρ.

$\lambda_0 \approx 1.5 \times 10^{-1}$ m, so the shock width, is about the same as the domain size. It is clear that the low value of collisionality has the effect of smearing out the shocks so that there are no longer three distinct regions, but a gradual transition to a higher density flow. At the moderate normal Mach number $M_{0n} = 1.3$, the distribution functions do not deviate heavily from Maxwellian, so both Navier-Stokes and 10-moment models capture the kinetic results well; as seen in the 1-D cases (i.e., Figs. 7(a–b)), the 10-moment results have slightly better agreement with DSMC than Navier-Stokes.

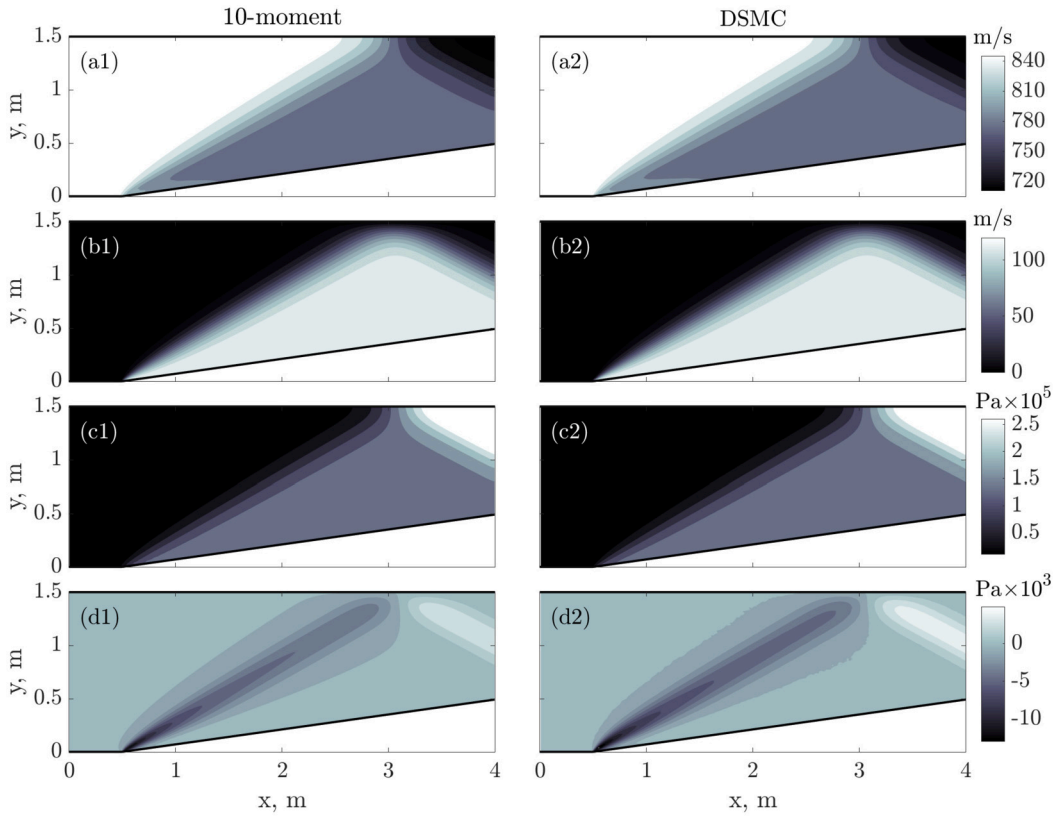

Fig. 13. Full (1) 10-moment and (2) DSMC results for the Mach 2.6 case with $\tau_0 = 1 \times 10^{-4}$ s (intermediate collisionality case), showing (a) u_x, (b) u_y, (c) p_{xx}, and (d) p_{xy}. See Fig. 11(b2) and (b3) for the profiles of ρ.

6.3. Fluid velocities and anisotropic pressure

Here, the other fluid properties, including x bulk velocity, y bulk velocity, p_{xx}, and p_{xy} are illustrated for high ($\tau_0 = 1 \times 10^{-5}$ s), intermediate ($\tau_0 = 1 \times 10^{-4}$ s), and low ($\tau_0 = 5 \times 10^{-4}$ s) collisionality cases.

Fig. 12 shows the high collisionality case. The results are close to the Euler solution where infinitely thin discontinuities separate distinct, uniform regions. The results presented follow the expectation, showing three uniform regions separated by oblique and reflected shocks which are both thin compared to the size of the regions. Flow is decelerated in the x direction, as shown in Fig. 12(a). The bulk velocity in y direction is zero in the regions before the first oblique shock (pre-shock) and after the reflected shock, but it is positive in the ramp region, as shown in Fig. 12(b). The pressure p_{xx} also shows discontinuous increase across the shocks (see Fig. 12(c)). Finally, Fig. 12(d) shows that non-zero off-diagonal pressure p_{xy} is captured in the shock layer. The existence of p_{xy} indicates that the direction of principal stress is not aligned with the coordinate axes. In the shock-oriented frame, the oblique shock looks like a normal shock: $p_{nn} > p_{tt}$ and $p_{nt} \approx 0$, where n and t are the normal and tangential directions to the oblique shock. Although there is no shear in the shock-oriented frame, the obliqueness of the directions of principal stress leads to a finite p_{xy} when the pressure tensor expressed in the lab-frame coordinates (x, y).

In the intermediate collisionality case, as shown in Fig. 13, we see roughly the same trend as with density showing a larger shock width, but we also begin to see some other features indicative of non-equilibrium effects. Right after the beginning of the ramp in Fig. 13(a), we note that there is a region of high x-velocity flow next to the wall that extends beyond the width of the shock. This can be explained by observing that at the corner of the ramp, all of the contours converge to a small width, and thus the shock is thinnest at this point. For this reason, it is likely some amount of high-speed low-collisionality flow can bend around the corner and penetrate further into the second region before being equilibrated. We note that the 10-moment solver is able to accurately capture this non-local effect seen in DSMC. The contours of y-velocity near the top wall, shown in Fig. 13(b), demonstrate the implementation of the no-penetration boundary condition (i.e., specular reflection), wherein the bulk y-velocity vanishes at the wall, and there is a finite region between the wall and the equilibrated flow as the shock reflects off of the upper wall. In addition, as shown in Fig. 13(c), the rise in pressure leads the rise in density (cf. Fig. 11) by a few λ_0, just as seen in Fig. 3. Furthermore, the magnitude and structure of p_{xy}, shown in Fig. 13(d), is captured accurately by the 10-moment model. The region of highest p_{xy} arising from the corner is captured, with p_{xy} decreasing with distance from the corner as the shock loses some of its strength. Finally, after the reflection of the shock, the sign of p_{xy} changes as the direction of shear reverses.

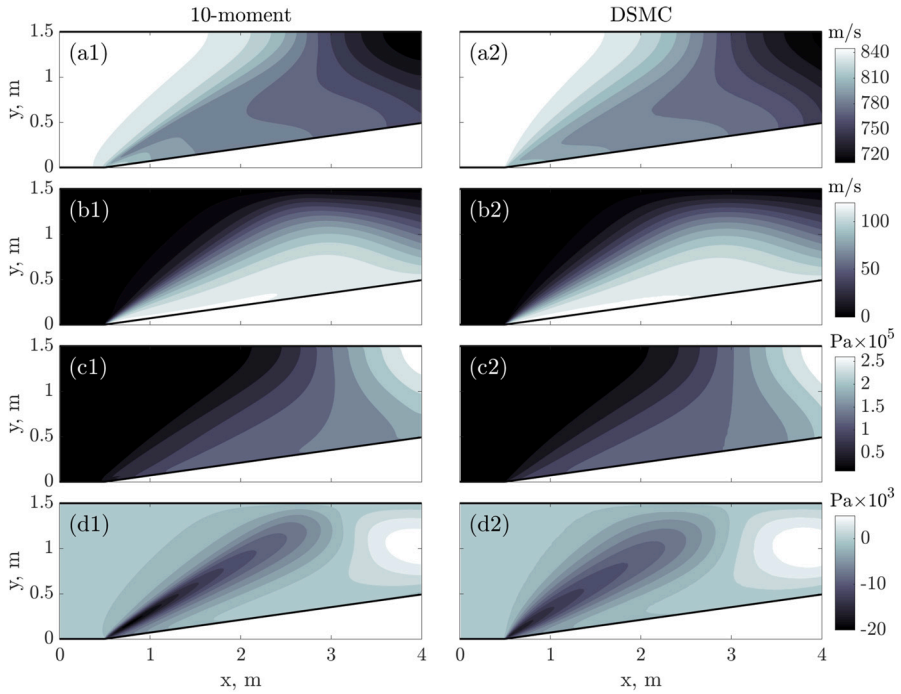

Fig. 14. Full (1) 10-moment and (2) DSMC results for the Mach 2.6 case with $\tau_0 = 5 \times 10^{-4}$ s (low collisionality case), showing (a) u_x, (b) u_y, (c) p_{xx}, and (d) p_{xy}. See Fig. 11(c2) and (c3) for the profiles of ρ.

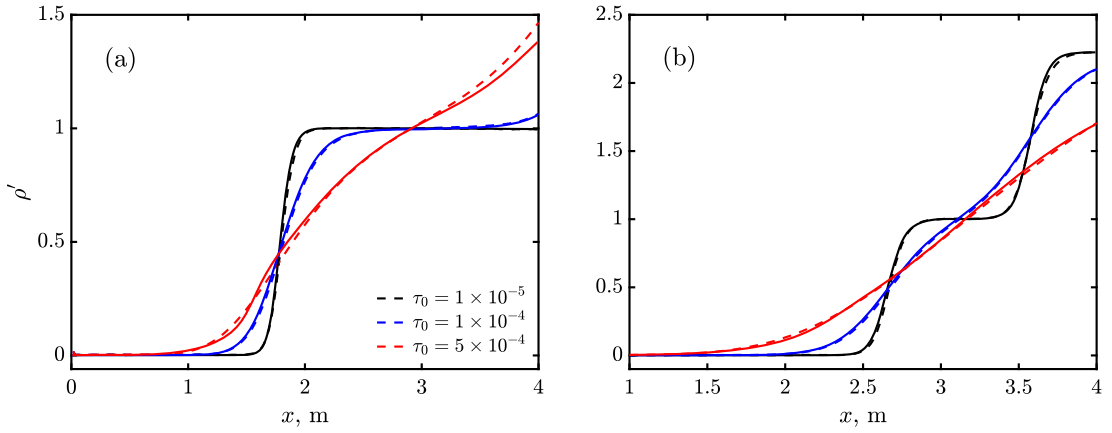

Fig. 15. Comparison of DSMC (dotted) and 10-moment (solid) density profiles for different degrees of collisionality, taking horizontal slices at (a) $y = 0.75$ m and (b) $y = 1.25$ m.

Finally, in the low collisionality case, i.e., in Fig. 14, we observe a greater broadening of the discontinuities, which then begin to interact with one another and are subject to highly nonequilibrium effects. As seen in Fig. 14(a), the 10-moment model is able to capture the high slip velocities after the corner near the wall of the ramp. Unlike in Fig. 13(a), where region of high velocity was equilibrated, at low collisionality, the region persists throughout the domain. A similar effect is visible in Fig. 14(b), which also showcases a region of high velocity near the ramp wall, as well as the extension of the shock width to encompass most of the width of the channel. The pressure contours in Fig. 14(c) also show excellent agreement between the 10-moment model and DSMC and also demonstrate that the two shocks are now indistinguishable, as the pressure increases smoothly throughout the domain as the flow is less collisional, i.e., more rarefied. Also, the contours of p_{xy}, as shown in Fig. 14(d) have increased in width and show good agreement in both magnitude and structure within the remnants of the shocks. Overall, there is good agreement on the width of the widened shock and the interaction of the two discontinuities with each other and the walls. However, there remain small discrepancies between the 10-moment and kinetic models, especially in the high Kn flow at the very start of the ramp, indicating that a higher-order model may be required to capture such effects.

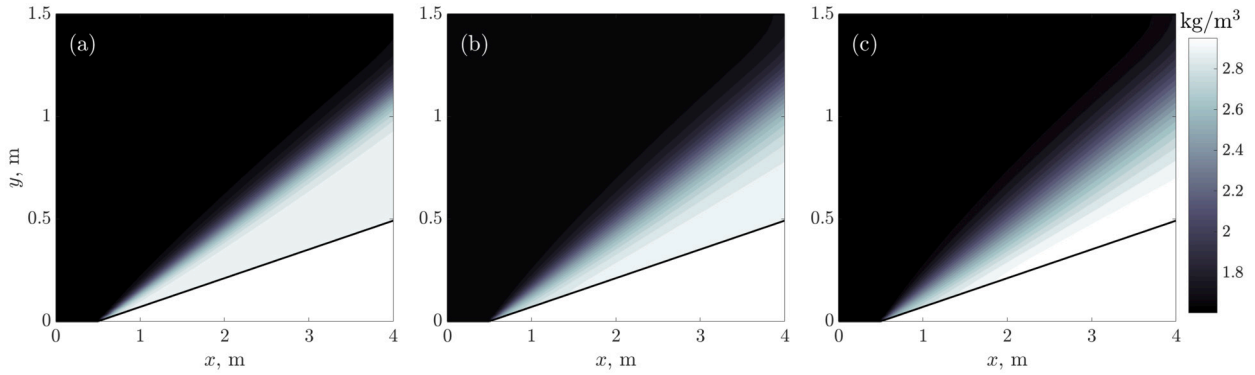

Fig. 16. Mass density profiles of the two dimensional ramp with incoming Mach number $M_L = 5.2$ ($M_n = 1.6$) oblique shock. The reference time $\tau_0 = 1 \times 10^{-4}$ s and we show a comparison between (a) Navier-Stokes, (b) 10-moment and (c) DSMC models.

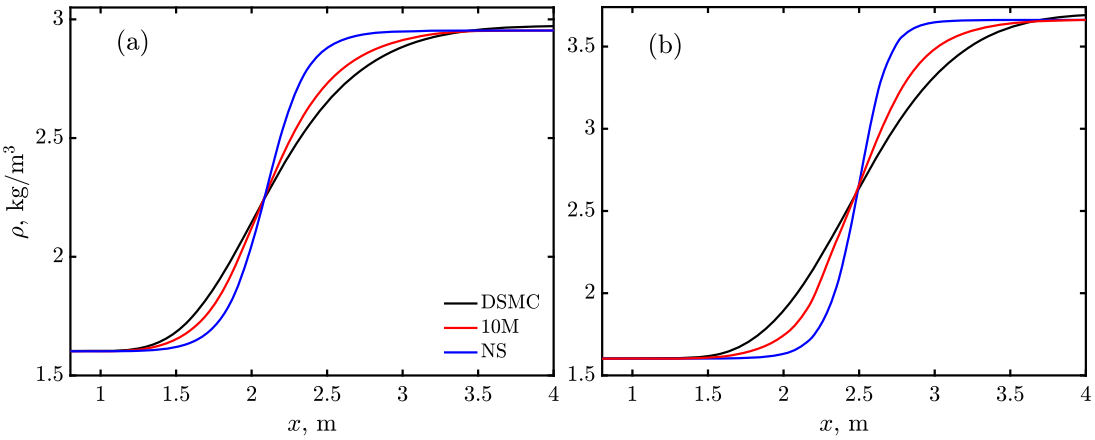

Fig. 17. Comparison of 10-moment, Navier-Stokes and DSMC density profiles at a horizontal slice at $y = 0.5$ m, for (a) $M_L = 5.2$, and (b) $M_L = 8$.

Fig. 15 shows horizontal cuts at $y = 0.75$ m and $y = 1.25$ m. Overall, the DSMC results and the 10-moment results are in good agreement. In Fig. 15(a), we note that at high collisionality ($\tau_0 = 1 \times 10^{-5}$ s), the reflected shock does not intersect the cut at $y = 0.75$ m, and so only the discontinuity due to the first oblique shock is observable. However, at the intermediate collisionality ($\tau_0 = 1 \times 10^{-4}$ s), not only does the first shock widen, but also the flow near the outflow boundary shows the effects of a widened reflected oblique shock. Finally, at low collisionality ($\tau_0 = 5 \times 10^{-4}$ s), the flow is rarefied so that the shock width becomes comparable to the size of the domain and the flow does not fully equilibrate. Likewise in Fig. 15(b), similar results are shown at $y = 1.25$ m, with shocks interacting in the intermediate collisionality case and then further broadening as collisionality decreases.

6.4. Higher Mach numbers

In order to provide a sharper distinction between the 10-moment and Navier-Stokes models in two spatial dimensions when the flow is further from equilibrium, we consider the same test problem with hypersonic incoming Mach numbers, $M_L = 5.2$ and $M_L = 8.0$, which correspond to normal Mach numbers of about $M_n = 1.6$ and $M_n = 2.0$, respectively. All values except for u_x, M_L are as noted in Table 4. The value of τ_0 is taken to be 3×10^{-4} s for all cases; because the shock will not reflect off the top wall in these cases, the system is scale-independent, and the width of the shock in DSMC is about $10\lambda_0$.

Fig. 16 shows a comparison of the mass density profiles between the Navier-Stokes, 10-moment and DSMC models for a Mach 5.2 oblique shock impinging on an 8° ramp. We see a similar trend to that found in Fig. 7, where at this higher Mach number, the Navier-Stokes solution, Fig. 16(a), significantly underestimates the width of the shock. Although the 10-moment model is not in as excellent agreement with DSMC as it was in the $M_L = 2.6$ test case, this clearly demonstrates the ability of the 10-moment model to out-perform the Navier-Stokes model in non-equilibrium regimes. As shown in the horizontal cuts of the density profile in Fig. 17, the trend is similar to in the one-dimensional case where, as the Mach number increases, the Navier-Stokes solution significantly underestimates the width of the shock while the 10-moment model is in imperfect, but superior agreement with DSMC.

One critical prediction of hypersonic flow simulations is the heat flux at the wall, since it informs design and material requirements. Although the focus of the present study is not the formation of boundary layers or the no-slip condition in the 10-moment model, we chose the wall-normal temperature gradient near the wall as a fluid property of interest to demonstrate the differences between the models in this 2-D test problem.

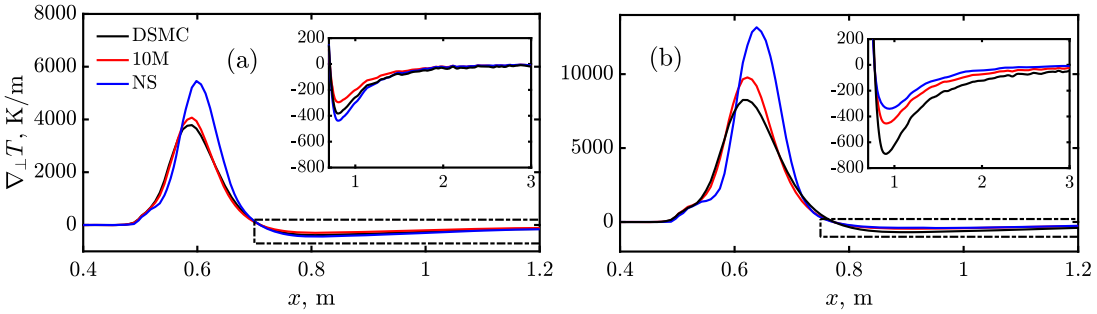

Fig. 18. Comparison of 10-moment, Navier-Stokes and DSMC wall-normal temperature gradients on the cell centers adjacent to the ramp and along the ramp for (a) $M_L = 5.2$, and (b) $M_L = 8$.

With the boundary condition described in Sections 3.2 and Appendix A and shown in Fig. 2, the gradient of isotropic temperature in the normal direction exactly at the wall interface should be zero at steady state. However, we can calculate a temperature gradient in the cells adjacent to the wall (i.e., the ramp) using the Green-Gauss method [66]

$$\vec{\nabla} T_{\text{ctr}} \simeq \frac{1}{A_{\text{ctr}}} \sum_{\text{int}} T_{\text{int}} \hat{n}_{\text{int}}, \tag{75}$$

where the interface value of the temperature is found using simple face averaging from the temperatures on the cell centers to either side of the interface, $T_{\text{int}} = \left(T_{\text{left}} + T_{\text{right}}\right)/2$. The wall-normal temperature gradient is then calculated as $\vec{\nabla} T \cdot \hat{n}_{\text{wall}}$ on the cell centers adjacent to the wall. The DSMC results are compared to fluid results with $[N_x, N_y] = [200, 75]$, using the same cell size between the kinetic and fluid simulations.

Fig. 18 shows a comparison of the cell-centered, wall-normal temperature gradient between the three models for incoming Mach numbers $M_L = 5.2$ and $M_L = 8$. We see that, due to underestimating the shock width, the Navier-Stokes model consistently overestimates the peak temperature gradient, and does not capture that the rise in temperature gradient occurs slightly further upstream, at $x \simeq 0.55$ m. In both cases, the 10-moment model provides a better estimate of the temperature gradient, and thus the heat flux within the shock. After the first oblique shock, there is a finite equilibration period for $x > 0.7$ m as the temperature relaxes to its equilibrium post-shock value. The contrast is not quite as stark in this region because the flow is nearer to equilibrium, but still the 10-moment model performs similarly to Navier-Stokes in approximating the DSMC profile in the post-shock wall region, particularly in the high Mach number condition, as shown in Fig. 18(b).

6.5. Grid convergence

In all of these presented results, the grid size is at least as fine as the mean free path in each region. To make sure that the grid resolution is high enough, a grid convergence study is conducted. The 10-moment results with $M_L = 2.6$ and $\tau_0 = 1 \times 10^{-6}$ s (fully collisional) are compared to the exact solution of the Euler equations. The normalized density is used as the metric for the grid convergence benchmark. The L_2 error norm is calculated as follows:

$$L_2 = \sqrt{\frac{1}{N} \sum_{\text{cell}=1}^{N} \left(\rho_{10M} - \rho_E\right)^2}, \tag{76}$$

where $N = N_x N_y$ is the total number of cells and ρ_{10M} and ρ_E are the solutions of the 10-moment and Euler models, respectively. Simulations were performed with $N_x = 100, 200, 300, 400$ and 600, with $N_y = 50, 75, 125, 150$, and 225, respectively. As the grid is not uniform in size in the domain, for demonstrative purposes, the average grid size is used:

$$(\Delta x)^2 = \frac{\text{Total Domain Area} \approx 5.14 \text{ m}^2}{N}. \tag{77}$$

Fig. 19 shows that the convergence is approximately first-order in Δx. This is to be expected because of the zeroth-order reconstruction for the interface values and interpolation of the cell values to cell interfaces for a non-orthogonal mesh. Nonetheless, the grid convergence demonstrates that the 10-moment solver is stable and provides a robust solution the gas dynamics problems in good agreement with kinetic DSMC results at a much lower computational cost.

7. Conclusions

In summary, the 10-moment model with Maxwellian heat flux closure provides a high-fidelity alternative to Navier-Stokes and higher-order moment simulations as its inviscid fluxes retain real eigenvalues for all initial conditions, and it is able to accurately capture finite kinetic effects. The model is shown to be in good agreement with DSMC simulations up to high Mach numbers, and up to Knudsen numbers on the order of 1. The 10-moment fluid model is formulated with a heat flux closure assuming relaxation

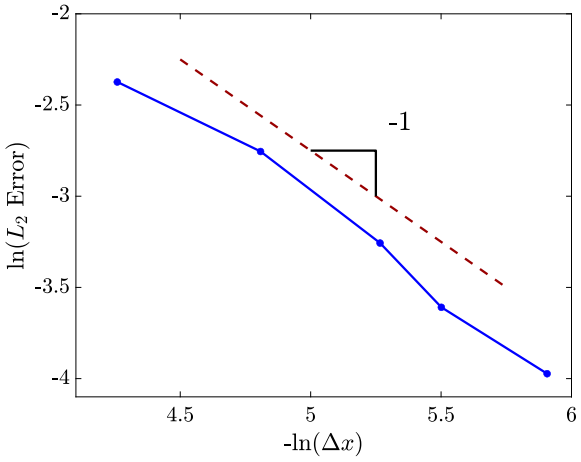

Fig. 19. The solid line shows the convergence rate in the 2-D case; the dashed line shows a first order convergence rate.

toward a Maxwellian distribution function. The 10-moment fluid model is compared with 5-moment (Navier-Stokes and Euler) and kinetic (DSMC) models for canonical problems. The resulting equation for heat flux provides values in each element of the rank 3 heat flux tensor in terms of the spatial derivatives of only the scalar temperature, and provide a low-complexity alternative to simple relaxation closures [39]. We postulate that the Maxwellian heat flux closure is more physically accurate than the Gaussian closure (cf. H-theorem). From the simulations, the 10-moment model with the Maxwellian closure is in better agreement with DSMC simulations than the 10-moment model with the Gaussian closure, despite the latter's incorporation of information from the full pressure tensor, demonstrating that the correct equilibrium distribution function should be the Maxwellian VDF for gas dynamics problems.

The 10-moment model inviscid fluxes are hyperbolic under all conditions and retain much of the simplicity of the inviscid Euler equations with the added benefit of being able to capture finite non-equilibrium effects. The 10-moment model is consistent with the Navier-Stokes equations at small Mach number and is in better agreement with DSMC as the Mach number and the shock-width Knudsen number $\mathrm{Kn}_s = \lambda / L_s$ increase. The superior performance of the 10-moment results stems from its ability to capture the effects of anisotropy and shear in non-Maxwellian VDFs in higher fidelity than the Navier-Stokes model.

The 10-moment results can show deviation from DSMC simulations when the distribution function is far from Maxwellian and kinetic effects dominate. Regardless, in a wide range of classic gasdynamic problems, the 10-moment model shows qualitatively good agreement with DSMC. More importantly, the robustness and convergence of the 10-moment model is illustrated in this paper. The model is also extended to two spatial dimensions, is able to capture finite non-local effects, and reproduce results similar to DSMC with low collisionality at a fraction of the computational cost.

Further work currently under way will apply this 10-moment system to electromagnetic fluids (plasmas) by adding further source terms where the external force term, $F_i \neq 0$ in Eqn. (1), which may require a different form of the closure. Furthermore, the collision operator can be extended to the more physically accurate Boltzmann operator, as well as to include inter-species collisions, both elastic (as in this paper) and inelastic excitation/ionization. This model could also be employed in hypersonics with reacting flows, which can become significantly rarefied and thus require the use of non-equilibrium models. For such cases, this model generalizes easily to unstructured grids in 3 spatial dimensions, using many of the techniques already developed for other fluid models.

CRediT authorship contribution statement

Derek A. Kuldinow: Conceptualization, Data curation, Formal analysis, Funding acquisition, Investigation, Methodology, Project administration, Resources, Software, Supervision, Validation, Visualization, Writing – original draft, Writing – review & editing. **Yusuke Yamashita:** Data curation, Formal analysis, Investigation, Methodology, Software, Validation, Writing – review & editing. **Adnan R. Mansour:** Conceptualization, Data curation, Writing – review & editing. **Kentaro Hara:** Conceptualization, Data curation, Funding acquisition, Investigation, Supervision, Writing – original draft, Writing – review & editing.

Declaration of competing interest

The authors declare the following financial interests/personal relationships which may be considered as potential competing interests: Derek Kuldinow reports financial support was provided by NASA. Derek Kuldinow reports financial support was provided by US Department of Energy. Kentaro Hara reports financial support was provided by NASA. Kentaro Hara reports financial support was provided by Office of Naval Research.

Data availability

Data will be made available on request.

Acknowledgements

The authors thank Shigemitsu Suzuki for his help in implementing the 1-dimensional Navier-Stokes simulations. This work was supported by a NASA Space Technology Graduate Research Opportunity, Grant No. 80NSSC21K1302, the U.S. Department of Energy National Nuclear Security Administration Stewardship Science Graduate Fellowship under cooperative agreement DE-NA0003960, NASA through the Joint Advanced Propulsion Institute, a NASA Space Technology Research Institute, under Grant No. 80NSSC21K1118, and the Office of Naval Research under Award No. N00014-21-1-2698. The authors would like to thank Stanford University and the Stanford Research Computing Center for providing computational resources and support that contributed to these research results. The authors would also like to thank the anonymous reviewers for their many helpful comments and suggestions which have improved the manuscript.

Appendix A. Eigendecomposition of 10-moment system

The eigendecomposition of the 10-moment system has been previously presented in other work [40,67], but for completeness, it is reproduced here.

Recall that the flux update to the conservative quantities can be written as

$$\frac{\partial \mathbf{U}}{\partial t} + \frac{\partial \mathbf{F}_i}{\partial x_i} = \frac{\partial \mathbf{U}}{\partial t} + \left(\frac{\partial \mathbf{F}_i}{\partial \mathbf{U}}\right)\frac{\partial \mathbf{U}}{\partial x_i} = 0 \tag{A.1}$$

where $\mathbf{U}$ is the vector of conservative variables, and $\mathbf{F}_i$ are the fluxes of the conservative variables in the i direction. For any i, disregarding the closure-based heat flux term, we have

$$\mathbf{U} = \begin{pmatrix} \rho \\ \rho u_x \\ \rho u_y \\ \rho u_z \\ \rho u_x^2 + p_{xx} \\ \rho u_x u_y + p_{xy} \\ \rho u_x u_z + p_{xz} \\ \rho u_y^2 + p_{yy} \\ \rho u_y u_z + p_{yz} \\ \rho u_z^2 + p_{zz} \end{pmatrix} \qquad \mathbf{F}_i = \begin{pmatrix} \rho u_i \\ \rho u_x u_i + p_{xi} \\ \rho u_y u_i + p_{yi} \\ \rho u_z u_i + p_{zi} \\ u_x p_{xi} + u_x p_{xi} + u_i \left(p_{xx} + \rho u_x u_x\right) \\ u_x p_{yi} + u_y p_{xi} + u_i \left(p_{xy} + \rho u_x u_y\right) \\ u_x p_{zi} + u_z p_{xi} + u_i \left(p_{xz} + \rho u_x u_z\right) \\ u_y p_{yi} + u_y p_{yi} + u_i \left(p_{yy} + \rho u_y u_y\right) \\ u_y p_{zi} + u_z p_{yi} + u_i \left(p_{yz} + \rho u_y u_z\right) \\ u_z p_{zi} + u_z p_{zi} + u_i \left(p_{zz} + \rho u_z u_z\right) \end{pmatrix}.$$

Without loss of generality, we can consider, in particular, the flux in the x direction. Then, the conservative flux Jacobian is

$$\frac{\partial \mathbf{F}_x}{\partial \mathbf{U}} = \begin{pmatrix} 0 & 1 & 0 & 0 & 0 & 0 & 0 & 0 & 0 & 0 \\ 0 & 0 & 0 & 0 & 1 & 0 & 0 & 0 & 0 & 0 \\ 0 & 0 & 0 & 0 & 0 & 1 & 0 & 0 & 0 & 0 \\ 0 & 0 & 0 & 0 & 0 & 0 & 1 & 0 & 0 & 0 \\ u^3 - 3up_{xx}/\rho & 3p_{xx}/\rho - 3u^2 & 0 & 0 & 3u & 0 & 0 & 0 & 0 & 0 \\ u^2 v - \left(2up_{xy} + vp_{xx}\right)/\rho & 2p_{xy}/\rho - 2uv & p_{xx}/\rho - u^2 & 0 & v & 2u & 0 & 0 & 0 & 0 \\ u^2 w - \left(2up_{xz} + wp_{xx}\right)/\rho & 2p_{xz}/\rho - 2uw & 0 & p_{xx}/\rho - u^2 & w & 0 & 2u & 0 & 0 & 0 \\ uv^2 - \left(2vp_{xy} + up_{yy}\right)/\rho & p_{yy}/\rho - v^2 & 2p_{xy}/\rho - 2uv & 0 & 0 & 2v & 0 & u & 0 & 0 \\ uvw - \left(up_{yz} + vp_{xz} + wp_{xy}\right)/\rho & p_{yz}/\rho - vw & p_{xz}/\rho - uw & p_{xy}/\rho - uv & 0 & w & v & 0 & u & 0 \\ uw^2 - \left(2wp_{xz} + up_{zz}\right)/\rho & p_{zz}/\rho - w^2 & 0 & 2p_{xz}/\rho - 2uw & 0 & 0 & 2w & 0 & 0 & u \end{pmatrix},$$

where we have defined that $\{u, v, w\} = \{u_x, u_y, u_z\}$. This complex matrix is difficult to work with; to aid in the eigendecomposition, we can express the Jacobian in terms of primitive variables through a change-of-basis, which will have the same characteristic speeds. Writing Eqn. (A.1) in primitive form,

$$\frac{\partial \mathbf{U}}{\partial \mathbf{\Pi}}\frac{\partial \mathbf{\Pi}}{\partial t} + \frac{\partial \mathbf{F}_x}{\partial \mathbf{U}}\frac{\partial \mathbf{U}}{\partial \mathbf{\Pi}}\frac{\partial \mathbf{\Pi}}{\partial x} = 0, \tag{A.2}$$

or equivalently,

$$\frac{\partial \mathbf{\Pi}}{\partial t} + \left[\left(\frac{\partial \mathbf{U}}{\partial \mathbf{\Pi}}\right)^{-1}\frac{\partial \mathbf{F}_x}{\partial \mathbf{U}}\frac{\partial \mathbf{U}}{\partial \mathbf{\Pi}}\right]\frac{\partial \mathbf{\Pi}}{\partial x} \equiv \frac{\partial \mathbf{\Pi}}{\partial t} + \mathbf{A}_x\frac{\partial \mathbf{\Pi}}{\partial x} = 0.$$

Using the change-of-basis matrix

$$\frac{\partial \mathbf{U}}{\partial \mathbf{\Pi}} = \begin{pmatrix} 1 & 0 & 0 & 0 & 0 & 0 & 0 & 0 & 0 & 0 \\ u & \rho & 0 & 0 & 0 & 0 & 0 & 0 & 0 & 0 \\ v & 0 & \rho & 0 & 0 & 0 & 0 & 0 & 0 & 0 \\ w & 0 & 0 & \rho & 0 & 0 & 0 & 0 & 0 & 0 \\ u^2 & 2\rho u & 0 & 0 & 1 & 0 & 0 & 0 & 0 & 0 \\ uv & \rho v & \rho u & 0 & 0 & 1 & 0 & 0 & 0 & 0 \\ uw & \rho w & 0 & \rho u & 0 & 0 & 1 & 0 & 0 & 0 \\ v^2 & 0 & 2\rho v & 0 & 0 & 0 & 0 & 1 & 0 & 0 \\ vw & 0 & \rho w & \rho v & 0 & 0 & 0 & 0 & 1 & 0 \\ w^2 & 0 & 0 & 2\rho w & 0 & 0 & 0 & 0 & 0 & 1 \end{pmatrix},$$

we obtain that the Jacobian under the transformation is

$$\mathbf{A}_x = \left[\left(\frac{\partial \mathbf{U}}{\partial \mathbf{\Pi}} \right)^{-1} \frac{\partial \mathbf{F}_x}{\partial \mathbf{U}} \frac{\partial \mathbf{U}}{\partial \mathbf{\Pi}} \right] = \begin{pmatrix} u & \rho & 0 & 0 & 0 & 0 & 0 & 0 & 0 & 0 \\ 0 & u & 0 & 0 & 1/\rho & 0 & 0 & 0 & 0 & 0 \\ 0 & 0 & u & 0 & 0 & 1/\rho & 0 & 0 & 0 & 0 \\ 0 & 0 & 0 & u & 0 & 0 & 1/\rho & 0 & 0 & 0 \\ 0 & 3p_{xx} & 0 & 0 & u & 0 & 0 & 0 & 0 & 0 \\ 0 & 2p_{xy} & p_{xx} & 0 & 0 & u & 0 & 0 & 0 & 0 \\ 0 & 2p_{xz} & 0 & p_{xx} & 0 & 0 & u & 0 & 0 & 0 \\ 0 & p_{yy} & 2p_{xy} & 0 & 0 & 0 & 0 & u & 0 & 0 \\ 0 & p_{yz} & p_{xz} & p_{xy} & 0 & 0 & 0 & 0 & u & 0 \\ 0 & p_{zz} & 0 & 2p_{xz} & 0 & 0 & 0 & 0 & 0 & u \end{pmatrix},$$

which is a much more sparse matrix than the original conservative Jacobian, but will have the same eigenvalues and eigenvectors. Performing the eigendecomposition on $\mathbf{A}_x$, we find the eigenvalues and right eigenvectors:

$$\lambda_{1,2,3,4} = u$$

$$\lambda_{5,7} = u + \sqrt{p_{xx}/\rho} \equiv u + c_1$$

$$\lambda_{6,8} = u - \sqrt{p_{xx}/\rho} \equiv u - c_1$$

$$\lambda_9 = u + \sqrt{3p_{xx}/\rho} \equiv u + c_2$$

$$\lambda_{10} = u - \sqrt{3p_{xx}/\rho} \equiv u - c_2$$

$$\vec{r}_1 = \begin{pmatrix} 1 \\ 0 \\ 0 \\ 0 \\ 0 \\ 0 \\ 0 \\ 0 \\ 0 \\ 0 \end{pmatrix} \vec{r}_2 = \begin{pmatrix} 0 \\ 0 \\ 0 \\ 0 \\ 0 \\ 0 \\ 0 \\ 1 \\ 0 \\ 0 \end{pmatrix} \vec{r}_3 = \begin{pmatrix} 0 \\ 0 \\ 0 \\ 0 \\ 0 \\ 0 \\ 0 \\ 0 \\ 1 \\ 0 \end{pmatrix} \vec{r}_4 = \begin{pmatrix} 0 \\ 0 \\ 0 \\ 0 \\ 0 \\ 0 \\ 0 \\ 0 \\ 0 \\ 1 \end{pmatrix} \vec{r}_5 = \begin{pmatrix} 0 \\ 0 \\ c_1 \\ 0 \\ 0 \\ p_{xx} \\ 0 \\ 2p_{xy} \\ p_{xz} \\ 0 \end{pmatrix} \vec{r}_6 = \begin{pmatrix} 0 \\ 0 \\ -c_1 \\ 0 \\ 0 \\ p_{xx} \\ 0 \\ 2p_{xy} \\ p_{xz} \\ 0 \end{pmatrix} \vec{r}_7 = \begin{pmatrix} 0 \\ 0 \\ 0 \\ c_1 \\ 0 \\ 0 \\ p_{xx} \\ 0 \\ p_{xy} \\ 2p_{xz} \end{pmatrix} \vec{r}_8 = \begin{pmatrix} 0 \\ 0 \\ 0 \\ -c_1 \\ 0 \\ 0 \\ p_{xx} \\ 0 \\ p_{xy} \\ 2p_{xz} \end{pmatrix}$$

$$\vec{r}_9 = \begin{pmatrix} \rho p_{xx} \\ c_2 p_{xx} \\ c_2 p_{xy} \\ c_2 p_{xz} \\ 3p_{xx}^2 \\ 3p_{xx}p_{xy} \\ 3p_{xx}p_{xz} \\ 2p_{xy}^2 + p_{xx}p_{yy} \\ 2p_{xy}p_{xz} + p_{xx}p_{yz} \\ 2p_{xz}^2 + p_{xx}p_{zz} \end{pmatrix} \vec{r}_{10} = \begin{pmatrix} \rho p_{xx} \\ -c_2 p_{xx} \\ -c_2 p_{xy} \\ -c_2 p_{xz} \\ 3p_{xx}^2 \\ 3p_{xx}p_{xy} \\ 3p_{xx}p_{xz} \\ 2p_{xy}^2 + p_{xx}p_{yy} \\ 2p_{xy}p_{xz} + p_{xx}p_{yz} \\ 2p_{xz}^2 + p_{xx}p_{zz} \end{pmatrix}.$$

Here, λ_1 corresponds to the entropy wave and, by observation of $\vec{r}_1$, advects variations in density. λ_{2-4} advect only transverse pressures p_{yy}, p_{yz}, and p_{zz} in the x direction and thus can be considered to be transverse pressure waves. $\lambda_{5,6}$ and $\lambda_{7,8}$ are shear waves in the y and z directions, respectively. These waves advect v and w in the x direction and propagate off-diagonal pressures as well. Finally, $\lambda_{9,10}$ are the fast acoustic waves, and by observation of $\vec{r}_{9,10}$ directly transport all of the primitive variables. It has been shown in other works [40] that these are the waves that reduce to the Euler sound waves in equilibrium.

We can also write down the conservative Steger-Warming fluxes,

$$\mathbf{F}^{\pm} = \frac{\partial \mathbf{U}}{\partial \mathbf{\Pi}} \mathbf{R} \mathbf{\Lambda}^{\pm} \mathbf{R}_{\mathbb{B}}^{-1} \left(\frac{\partial \mathbf{U}}{\partial \mathbf{\Pi}} \right)^{-1} \mathbf{U},$$

where $\mathbf{R} = \left[\vec{r}_1, \ldots \vec{r}_{10} \right]$ is the matrix of right eigenvectors and $\mathbf{\Lambda}^{\pm}$ is the diagonal matrix of leftward/rightward eigenvalues where $\Lambda^{\pm}_{i,i} = \lambda^{\pm}_i$. For the original Steger-Warming scheme, $\lambda^{\pm} = \frac{1}{2}(\lambda \pm |\lambda|)$. Performing the matrix operations yields $\mathbf{F}^{\pm}_x =$

$$\frac{1}{6} \begin{pmatrix} \rho \left(4\lambda_1^{\pm} + \lambda_9^{\pm} + \lambda_{10}^{\pm} \right) \\ 4\rho u \lambda_1^{\pm} + \rho c_2 \left(M_u + 1 \right) \lambda_9^{\pm} + \rho c_2 \left(M_u - 1 \right) \lambda_{10}^{\pm} \\ 4\rho v \lambda_1^{\pm} + \left(\rho v + 3\frac{p_{xy}}{c_2} \right) \lambda_9^{\pm} + \left(\rho v - 3\frac{p_{xy}}{c_2} \right) \lambda_{10}^{\pm} \\ 4\rho w \lambda_1^{\pm} + \left(\rho w + 3\frac{p_{xz}}{c_2} \right) \lambda_9^{\pm} + \left(\rho w - 3\frac{p_{xz}}{c_2} \right) \lambda_{10}^{\pm} \\ 4\rho u^2 \lambda_1^{\pm} + \left(\rho u^2 + 2\rho u c_2 + 3p_{xx} \right) \lambda_9^{\pm} + \left(\rho u^2 - 2\rho u c_2 + 3p_{xx} \right) \lambda_{10}^{\pm} \\ 4\rho uv \lambda_1^{\pm} + (3p_{xy} + \rho v c_2)(1 + M_u) \lambda_9^{\pm} + \left(3p_{xy} - \rho v c_2 \right)(1 - M_u) \lambda_{10}^{\pm} \\ 4\rho uw \lambda_1^{\pm} + (3p_{xz} + \rho w c_2)(1 + M_u) \lambda_9^{\pm} + (3p_{xz} - \rho w c_2)(1 - M_u) \lambda_{10}^{\pm} \\ 4\rho v^2 \lambda_1^{\pm} + 4\left(p_{yy} - \frac{p_{xy}^2}{p_{xx}} \right) \lambda_1^{\pm} + \left(2\frac{p_{xy}^2}{p_{xx}} + p_{yy} + 6p_{xy} M_v + \rho v^2 \right) \lambda_9^{\pm} + \left(2\frac{p_{xy}^2}{p_{xx}} + p_{yy} - 6p_{xy} M_v + \rho v^2 \right) \lambda_{10}^{\pm} \\ 4\rho vw \lambda_1^{\pm} + 4\left(p_{yz} - \frac{p_{xy} p_{xz}}{p_{xx}} \right) \lambda_1^{\pm} + \left(2\frac{p_{xy} p_{xz}}{p_{xx}} + p_{yz} + 3p_{xz} M_v + 3p_{xy} M_w + \rho vw \right) \lambda_9^{\pm} + \cdots \\ \cdots + \left(2\frac{p_{xy} p_{xz}}{p_{xx}} + p_{yz} - 3p_{xz} M_v - 3p_{xy} M_w + \rho vw \right) \lambda_{10}^{\pm} \\ 4\rho w^2 \lambda_1^{\pm} + 4\left(p_{zz} - \frac{p_{xz}^2}{p_{xx}} \right) \lambda_1^{\pm} + \left(2\frac{p_{xz}^2}{p_{xx}} + p_{zz} + 6p_{xz} M_w + \rho w^2 \right) \lambda_9^{\pm} + \left(2\frac{p_{xz}^2}{p_{xx}} + p_{zz} - 6p_{xz} M_w + \rho w^2 \right) \lambda_{10}^{\pm} \end{pmatrix},$$

where we have defined $M_{u,v,w} \equiv (u, v, w)/c_2$.

Appendix B. Details of 2-dimensional wall boundary condition

Recall that in two dimensions, the approximate Gaussian distribution in two velocity dimensions is

$$f^{2D} \simeq \frac{\rho}{m} \left[\frac{\rho^2}{(2\pi)^2 \left(p_{xx} p_{yy} - p_{xy}^2 \right)} \right]^{1/2} \exp \left[-\frac{\rho}{p_{xx} p_{yy} - p_{xy}^2} \left(p_{yy} w_x^2 - 2p_{xy} w_x w_y + p_{xx} w_y^2 \right) \right],$$

where the argument of the exponential can be written in the form of the general ellipse,

$$K \left(p_{yy} w_x^2 - 2p_{xy} w_x w_y + p_{xx} w_y^2 \right) = A w_x^2 + B w_x w_y + C w_y^2 \tag{B.1}$$

Then the angle of the major axis of the ellipsoidal distribution function, i.e., the principal stress direction, to the x direction is

$$\theta = \tan^{-1} \left(\frac{C - A - \sqrt{(A - C)^2 + B^2}}{B} \right). \tag{B.2}$$

Furthermore, the semimajor and semiminor axes a, b are

$$a, b = \frac{\sqrt{2\left(4AC - B^2\right)\left[(A + C) \pm \sqrt{(A - C)^2 + B^2}\right]}}{4AC - B^2}.$$

After collision with a wall of angle ϕ to the x direction, this angle must be reflected about the wall so

$$\theta_{post} = 2\phi - \theta_{pre},$$

as shown in Fig. 2. Then, to reconstruct the post-collision pressures, we use generalized ellipse identities:

$$A_{post} = a^2 \sin^2 \left(\theta_{post} \right) + b^2 \cos^2 \left(\theta_{post} \right)$$
$$B_{post} = 2\left(b^2 - a^2 \right) \sin \left(\theta_{post} \right) \cos \left(\theta_{post} \right)$$
$$C_{post} = a^2 \cos^2 \left(\theta_{post} \right) + b^2 \sin^2 \left(\theta_{post} \right).$$

Finally, back-substituting these into Eqn. (B.1) yields the post-collision pressures.

This method can be extended to three dimensions by considering transforming into the plane spanned by the bulk velocity $\mathbf{u}$ and the wall normal $\hat{\mathbf{n}}$. In this case, a similar algorithm for a generalized 3-D ellipsoid may be used.

This method can also be extended to include an accommodation coefficient α by mixing the specularly reflected VDF with an isotropic diffusely reflected VDF,

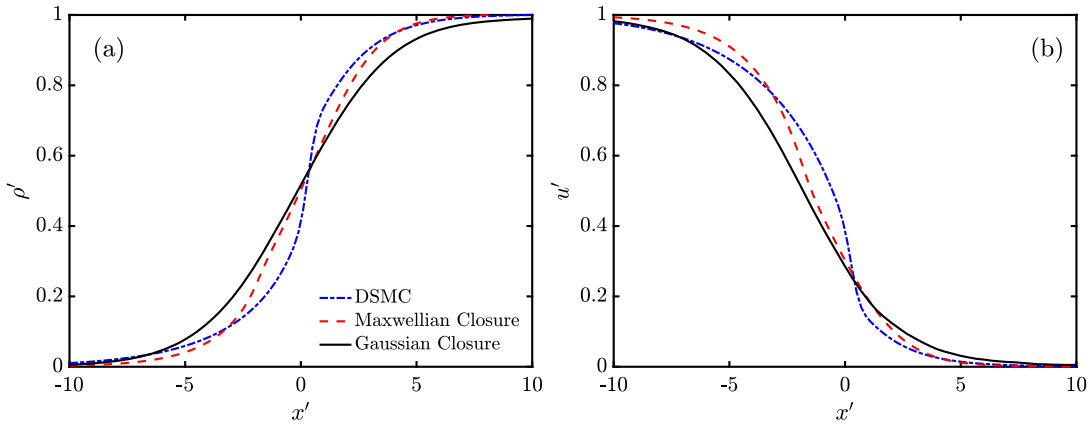

Fig. 20. Comparison of DSMC to 10-moment fluid results using Maxwellian and Gaussian for Chapman-Enskog expansion showing (a) p'_{xx} and (b) p'_{yy} in a Mach 2 normal shock.

$$f^{\text{reflected}} = \alpha f^{\text{diffuse}} + (1-\alpha) f^{\text{specular}}, \tag{B.3}$$

where f^{specular} is calculated as above and f^{diffuse} is the stationary Maxwellian distribution function where $\{\rho, u_i, p\}^{\text{post,diffuse}} = \{\rho, 0, (p + \rho u^2/3)\}^{\text{pre}}$. The results in this study only consider $\alpha = 0$, that is, a fully specular boundary condition; a rigorous testing of this boundary condition is left for future work.

Appendix C. Extended comparison between 10-moment Gaussian and Maxwellian closures

For completeness, Fig. 20 presents an extension of Fig. 6 to include the profiles of ρ and u_x to demonstrate that the heat flux closure affects all of the flow variables.

The indirect effect of the heat flux on density and velocity can be thought of in two ways. Firstly, by directly affecting pressure, it affects the wavespeeds and thus the eigenvector transport. Since sound-speed dependent eigenvectors $\left(\lambda_{5-10}\right)$ transport all of the flow variables, the heat flux does so also. Secondly, by affecting the pressure profile, this changes the momentum flux, affecting velocity, which affects mass flux. In short, higher-order moments are the flux of the next-highest moment, and so differences in the highest moment (heat flux) can climb up the chain of moments and affect the profiles of all of the flow variables.

References

[1] W.G. Vincenti, C.H. Kruger, Introduction to physical gas dynamics, J. R. Aeronaut. Soc. 70 (667) (1966) 741–742.
[2] I.G. Mikellides, I. Katz, Numerical simulations of Hall-effect plasma accelerators on a magnetic-field-aligned mesh, Phys. Rev. E 86 (2012) 046703.
[3] M.A. Lieberman, A.J. Lichtenberg, Principles of Plasma Discharges and Materials Processing, John Wiley & Sons, 2005.
[4] M.S. Ivanov, S.F. Glimelshein, Computational hypersonic rarefied flows, Annu. Rev. Fluid Mech. 30 (1998) 469.
[5] L. Tonks, Oscillations in ionized gases, in: Plasma and Oscillations, Elsevier, 1961, pp. 122–139.
[6] A.H. Hakim, Extended MHD modelling with the ten-moment equations, J. Fusion Energy 27 (2008) 36–43.
[7] V.M. Zhdanov, Transport Processes in Multicomponent Plasma, CRC Press, 2002.
[8] H. Grad, On the kinetic theory of rarefied gases, Commun. Pure Appl. Math. 2 (4) (1949) 331–407.
[9] H. Grad, Principles of the kinetic theory of gases, in: Thermodynamik der Gase/Thermodynamics of Gases, Springer, 1958, pp. 205–294.
[10] P.L. Bhatnagar, E.P. Gross, M. Krook, A model for collision processes in gases. I. Small amplitude processes in charged and neutral one-component systems, Phys. Rev. 94 (3) (1954) 511.
[11] L.H. Holway Jr., New statistical models for kinetic theory: methods of construction, Phys. Fluids 9 (9) (1966) 1658–1673.
[12] C.D. Levermore, Moment closure hierarchies for kinetic theories, J. Stat. Phys. 83 (5) (1996) 1021–1065.
[13] M. Torrilhon, Modeling nonequilibrium gas flow based on moment equations, Annu. Rev. Fluid Mech. 48 (2016) 429–458.
[14] W. Dreyer, Maximisation of the entropy in non-equilibrium, J. Phys. A, Math. Gen. 20 (18) (1987) 6505.
[15] B. Biswas, H. Kumar, A. Yadav, Entropy stable discontinuous Galerkin methods for ten-moment Gaussian closure equations, J. Comput. Phys. 431 (2021) 110148.
[16] C. Yan, J.G. McDonald, Hyperbolic turbulence models for moment closures, J. Comput. Phys. 422 (2020) 109753.
[17] L. Wang, A.H. Hakim, J. Juno, B. Srinivasan, Electron cyclotron drift instability and anomalous transport: two-fluid moment theory and modeling, Plasma Sources Sci. Technol. 31 (10) (2022) 105001.
[18] Patrick Le Tallec, Jean-Philippe Perlat, Numerical analysis of Levermore's moment system, PhD thesis, Inria, 1997.
[19] Z. Cai, Y. Fan, R. Li, On hyperbolicity of 13-moment system, arXiv preprint, arXiv:1401.7523, 2014.
[20] Toby Thatcher, Y. Zheng, H. Struchtrup, Boundary conditions for Grad's 13 moment equations, Prog. Comput. Fluid Dyn. 8 (1–4) (2008) 69–83.
[21] H. Struchtrup, M. Torrilhon, Regularization of Grad's 13 moment equations: derivation and linear analysis, Phys. Fluids 15 (9) (2003) 2668–2680.
[22] Manuel Torrilhon, Henning Struchtrup, Boundary conditions for regularized 13-moment-equations for micro-channel-flows, J. Comput. Phys. 227 (3) (2008) 1982–2011.
[23] M. Torrilhon, Hyperbolic moment equations in kinetic gas theory based on multi-variate Pearson-IV-distributions, Commun. Comput. Phys. 7 (4) (2010) 639.
[24] R. McGraw, Description of aerosol dynamics by the quadrature method of moments, Aerosol Sci. Technol. 27 (2) (1997) 255–265.
[25] O. Desjardins, Rodney R.O. Fox, P. Villedieu, A quadrature-based moment method for dilute fluid-particle flows, J. Comput. Phys. 227 (4) (2008) 2514–2539.
[26] C. Yuan, Frédérique Laurent, R.O. Fox, An extended quadrature method of moments for population balance equations, J. Aerosol Sci. 51 (2012) 1–23.
[27] Pierre-Yves CR Taunay, Michael E. Mueller, Quadrature-based moment methods for kinetic plasma simulations, J. Comput. Phys. 473 (2023) 111700.

[28] Rodney O. Fox, Frédérique Laurent, Aymeric Vié, Conditional hyperbolic quadrature method of moments for kinetic equations, J. Comput. Phys. 365 (2018) 269–293.
[29] S. Boccelli, F. Giroux, T.E. Magin, C.P.T. Groth, J.G. McDonald, A 14-moment maximum-entropy description of electrons in crossed electric and magnetic fields, Phys. Plasmas 27 (12) (2020) 123506.
[30] S. Boccelli, Moment methods for non-equilibrium low-temperature plasmas with application to electric propulsion, 2021.
[31] J.G. McDonald, C. Groth, Towards realizable hyperbolic moment closures for viscous heat-conducting gas flows based on a maximum-entropy distribution, Contin. Mech. Thermodyn. 25 (5) (2013) 573–603.
[32] M. Junk, Domain of definition of Levermore's five-moment system, J. Stat. Phys. 93 (5) (1998) 1143–1167.
[33] M. Junk, A. Unterreiter, Maximum entropy moment systems and Galilean invariance, Contin. Mech. Thermodyn. 14 (6) (2002) 563–576.
[34] K. Hara, An overview of discharge plasma modeling for Hall effect thrusters, Plasma Sources Sci. Technol. 28 (4) (2019) 044001.
[35] M.J. Kushner, Hybrid modelling of low temperature plasmas for fundamental investigations and equipment design, J. Phys. D, Appl. Phys. 42 (19) (2009) 194013.
[36] Gregory W. Hammett, Francis W. Perkins, Fluid moment models for Landau damping with application to the ion-temperature-gradient instability, Phys. Rev. Lett. 64 (25) (1990) 3019.
[37] G.W. Hammett, W. Dorland, F.W. Perkins, Fluid models of phase mixing, Landau damping, and nonlinear gyrokinetic dynamics, Phys. Fluids, B Plasma Phys. 4 (7) (1992) 2052–2061.
[38] P.B. Snyder, G.W. Hammett, W. Dorland, Landau fluid models of collisionless magnetohydrodynamics, Phys. Plasmas 4 (11) (1997) 3974–3985.
[39] L. Wang, A.H. Hakim, A. Bhattacharjee, K. Germaschewski, Comparison of multi-fluid moment models with particle-in-cell simulations of collisionless magnetic reconnection, Phys. Plasmas 22 (1) (2015) 012108.
[40] S. Brown, P. Roe, C.P.T. Groth, Numerical solution of a 10-moment model for nonequilibrium gasdynamics, in: 12th Computational Fluid Dynamics Conference, 1995, p. 1677.
[41] S. Chapman, T.G. Cowling, The Mathematical Theory of Non-uniform Gases: An Account of the Kinetic Theory of Viscosity, Thermal Conduction and Diffusion in Gases, Cambridge University Press, 1990.
[42] A. Alvarez Laguna, B. Esteves, A. Bourdon, P. Chabert, A regularized high-order moment model to capture non-Maxwellian electron energy distribution function effects in partially ionized plasmas, Phys. Plasmas 29 (8) (2022) 083507.
[43] S. Chapman, T.G. Cowling, The mathematical theory of non uniform gases, Cambridge, 2e éd. I 952 (1970) 354–356.
[44] P. Andries, B. Perthame, The ES-BGK Model Equation with Correct Prandtl Number, AIP Conference Proceedings, vol. 585, American Institute of Physics, 2001, pp. 30–36.
[45] M. Becker, D. Loffhagen, Derivation of moment equations for the theoretical description of electrons in nonthermal plasmas, 2013.
[46] J. McDonald, M. Torrilhon, Affordable robust moment closures for CFD based on the maximum-entropy hierarchy, J. Comput. Phys. 251 (2013) 500–523.
[47] E.A. Johnson, Gaussian-moment relaxation closures for verifiable numerical simulation of fast magnetic reconnection in plasma, arXiv preprint, arXiv:1409.6985, 2014.
[48] F. Allmann-Rahn, T. Trost, R. Grauer, Temperature gradient driven heat flux closure in fluid simulations of collisionless reconnection, J. Plasma Phys. 84 (3) (2018).
[49] H. Struchtrup, Macroscopic Transport Equations for Rarefied Gas Flows: Approximation Methods in Kinetic Theory, Springer Science & Business Media, 2005.
[50] L. Mieussens, H. Struchtrup, Numerical comparison of Bhatnagar-Gross-Krook models with proper Prandtl number, Phys. Fluids 16 (8) (2004) 2797–2813.
[51] I.D. Boyd, T.E. Schwartzentruber, Nonequilibrium Gas Dynamics and Molecular Simulation, Cambridge Aerospace Series, Cambridge University Press, 2017.
[52] G.A. Bird, Molecular gas dynamics and the direct simulation of gas flows, in: Molecular Gas Dynamics and the Direct Simulation of Gas Flows, 1994.
[53] H. Alsmeyer, Density profiles in argon and nitrogen shock waves measured by the absorption of an electron beam, J. Fluid Mech. 74 (3) (1976) 497–513.
[54] S. Gottlieb, C. Shu, E. Tadmor, Strong stability-preserving high-order time discretization methods, SIAM Rev. 43 (1) (2001) 89–112.
[55] R. Sahu, A.R. Mansour, K. Hara, Full fluid moment model for low temperature magnetized plasmas, Phys. Plasmas 27 (11) (2020) 113505.
[56] J.L. Steger, R.F. Warming, Flux vector splitting of the inviscid gasdynamic equations with application to finite-difference methods, J. Comput. Phys. 40 (2) (1981) 263–293.
[57] B. van Leer, Towards the ultimate conservative difference scheme. V. A second-order sequel to Godunov's method, J. Comput. Phys. 32 (1) (1979) 101–136.
[58] S.L. Brown, Approximate Riemann Solvers for Moment Models of Dilute Gases, PhD thesis, University of Michigan, 1996.
[59] C.D. Levermore, W.J. Morokoff, The Gaussian moment closure for gas dynamics, SIAM J. Appl. Math. 59 (1) (1998) 72–96.
[60] C. Groth, J.G. McDonald, Towards physically realizable and hyperbolic moment closures for kinetic theory, Contin. Mech. Thermodyn. 21 (6) (2009) 467–493.
[61] James G. McDonald, Extended Fluid-Dynamic Modelling for Numerical Solution of Micro-Scale Flows, University of Toronto, 2011.
[62] G.A. Sod, A survey of several finite difference methods for systems of nonlinear hyperbolic conservation laws, J. Comput. Phys. 27 (1) (1978) 1–31.
[63] S. Jaiswal, Isogeometric schemes in rarefied gas dynamics context, Comput. Methods Appl. Mech. Eng. 383 (2021) 113926.
[64] K. Xu, J. Huang, A unified gas-kinetic scheme for continuum and rarefied flows, J. Comput. Phys. 229 (20) (2010) 7747–7764.
[65] K. Xu, Q. Sun, P. Yu, Valid physical processes from numerical discontinuities in computational fluid dynamics, arXiv preprint, arXiv:1009.4326, 2010.
[66] Emre Sozer, Christoph Brehm, Cetin C. Kiris, Gradient calculation methods on arbitrary polyhedral unstructured meshes for cell-centered cfd solvers, in: 52nd Aerospace Sciences Meeting, 2014, p. 1440.
[67] C. Berthon, B. Dubroca, A. Sangam, An entropy preserving relaxation scheme for ten-moments equations with source terms, Commun. Math. Sci. 13 (8) (2015) 2119–2154.